Integrated Multi-Omics and Interactome Analysis of CDK8 Inhibition Reveals Erythroid Differentiation Programs and BET Synergy in AML Stem-like Cells

Małgorzata Statkiewicz
Narodowy Instytut Onkologii im Marii Sklodowskiej-Curie Panstwowy Instytut Badawczy w Warszawie
Izabela Rumienczyk
Narodowy Instytut Onkologii im Marii Sklodowskiej-Curie Panstwowy Instytut Badawczy w Warszawie
Urszula Pakulska
Ryvu Therapeutics
Marta Obacz
Ryvu Therapeutics
Maria Kulecka
Centre of Postgraduate Medical Education
Jaroslaw Cendrowski
Narodowy Instytut Onkologii im Marii Sklodowskiej-Curie Panstwowy Instytut Badawczy w Warszawie
Magdalena Cubulska-Lubak
Narodowy Instytut Onkologii im Marii Sklodowskiej-Curie Panstwowy Instytut Badawczy w Warszawie
Ewelina Kaniuga
Narodowy Instytut Onkologii im Marii Sklodowskiej-Curie Panstwowy Instytut Badawczy w Warszawie
Zuzanna Sandowska-Markiewicz
Narodowy Instytut Onkologii im Marii Sklodowskiej-Curie Panstwowy Instytut Badawczy w Warszawie
Wioletta Slusarczyk-Kacprzyk
Narodowy Instytut Onkologii im Marii Sklodowskiej-Curie Panstwowy Instytut Badawczy w Warszawie
Krzysztof Goryca
University of Warsaw Centre of New Technologies: Uniwersytet Warszawski Centrum Nowych Technologii
Tymon Rubel
Politechnika Warszawska Wydzial Elektroniki i Technik Informacyjnych
Magdalena Bakun
Instytut Biochemii i Biofizyki Polskiej Akademii Nauk
Bianka Swiderska
Instytut Biochemii i Biofizyki Polskiej Akademii Nauk
Kamila Kruczkowska-Tarantowicz

Wojskowy Instytut Medyczny - Państwowy Instytut Badawczy: Wojskowy Instytut Medyczny - Panstwowy Instytut Badawczy

Piotr Rzepecki
Wojskowy Instytut Medyczny - Państwowy Instytut Badawczy: Wojskowy Instytut Medyczny - Panstwowy Instytut Badawczy

Jolanta Korsak
Wojskowy Instytut Medyczny - Państwowy Instytut Badawczy: Wojskowy Instytut Medyczny - Panstwowy Instytut Badawczy

Krystyna Kyc-Wachowiak
Wojskowy Instytut Medyczny - Państwowy Instytut Badawczy: Wojskowy Instytut Medyczny - Panstwowy Instytut Badawczy

Anna Polak
Instytut Hematologii i Transfuzjologii

Przemyslaw Juszczynski
Instytut Hematologii i Transfuzjologii

Milena Mazan
Ryvu Therapeutics

Tomasz Rzymski
Ryvu Therapeutics

Jerzy Ostrowski
Narodowy Instytut Onkologii im Marii Sklodowskiej-Curie Panstwowy Instytut Badawczy w Warszawie

Michal Mikula
Michal.Mikula@nio.gov.pl

Narodowy Instytut Onkologii im Marii Sklodowskiej-Curie Panstwowy Instytut Badawczy w Warszawie
https://orcid.org/0000-0003-3447-7328

Research Article

Keywords: Leukemic Stem Cells, CDK8 inhibitor, protein-protein interactome, chromatin remodelling, BET-CDK8 synergy

Posted Date: March 26th, 2026

DOI: https://doi.org/10.21203/rs.3.rs-8989018/v1

Abstract

Background.

Acute myeloid leukemia (AML) remains among the most therapeutically challenging hematologic malignancies, driven largely by the self-renewal capacity, quiescence, and therapy resistance of leukemic stem cells (LSCs). CDK8, a kinase component of the Mediator complex, has emerged as a regulator of oncogenic transcription. We demonstrated that the selective CDK8/CDK19 inhibitor RVU120 (Romaciclib; SEL120-34A) potently targets AML cells with CD34^{+}/pSTAT5-high LSC-like characteristics. However, the full spectrum of epigenetic and transcriptional events triggered by CDK8 blockade, and combinatorial strategies that may exploit them, remains incompletely defined.

Methods.

Using the TEX LSC-like cell line treated with CDK8 inhibitors, RVU120 and CCT251921, we performed time-resolved (3h, 24h, 72h) RNA-Seq, whole-proteome and phosphoproteomics mass spectrometry (MS). Chromatin occupancy of CDK8, Polymerase II RNA (RNAP2), BRD3, MLL-4, NFRKB and histone marks (H3K27ac, H3K4me1, H3K4me3) was profiled with CUT&Tag. CDK8 protein–protein interactions (PPIs) were surveyed by co-immunoprecipitation MS (co-IP-MS) and validated across five AML models. Synergy between CDK8 inhibitors and Pelabresib (BET inhibitor) or CB6644 (RUVBL1/2 inhibitor) was assessed by high-content screening microscopy in three cell lines and three patient-derived xenograft (PDX) models.

Results.

Both inhibitors suppressed STAT5 Ser726/731 phosphorylation; over subsequent days, TEX cells lost their CD34^{+}/CD38^{-} phenotype and acquired surface markers of erythromegakaryocytic differentiation. Transcriptomics revealed a concordant response to both CDK8 inhibitors (r = 0.82–0.95), including early cholesterol biosynthesis, followed by inflammatory programs, and erythroid commitment with GATA1 upregulation. Whole-proteome changes significantly correlated with the transcriptomic response (r = 0.65–0.78). Phosphoproteomics identified 33 significantly different phosphosites with overrepresentation of nucleic acid-binding proteins. In the TEX cell line, co-IP-MS identified 125 CDK8-interacting proteins and a conserved PPI network across five AML models, including Mediator subunits, NFRKB, and BRD3. CUT&Tag genomic profiling demonstrated that CDK8 inhibition triggers widespread enhancer activation with coordinated redistribution of RNAP2, BRD3, and NFRKB, while uncoupling proliferative from immune-regulatory chromatin programs. CDK8 combined with Pelabresib acted synergistic in MOLM-16 cells and two of three PDX models.

Conclusions.

These findings position CDK8 as a central node in LSC transcriptional control and establish a mechanistic rationale for combined CDK8-BET inhibition as a precision therapeutic strategy in molecularly defined AML subsets.

Background

Acute myeloid leukemia (AML) continues to pose significant challenges in clinical treatment, despite progress with targeted and traditional therapies. One of the main obstacles to achieving long-lasting remission is the presence of leukemic stem cells (LSCs), a primitive group of progenitor cells that drive the disease through their ability to self-renew, remain quiescent within protective microenvironmental niches, and resist differentiation [1, 2]. Unlike the bulk of leukemic blasts, LSCs often display primitive surface markers, such as CD34, and exhibit elevated activity in pathways that support stemness, including STAT5 activation [3]. A key goal of AML therapy is to selectively eliminate LSCs while sparing normal hematopoietic stem and progenitor cells, since LSCs are believed to be the main source of relapse and treatment resistance in most patients [4]. Recent insights from functional genomics and chemical biology have highlighted the Mediator kinase module, especially cyclin-dependent kinase 8 (CDK8), as a crucial transcriptional regulator in AML. CDK8, along with CDK19, Cyclin C, and MED12, forms the core of this complex and plays an important role in controlling both cancer-related transcription and normal blood cell development [5, 6]. It functions as a versatile kinase that influences RNA polymerase II (RNAP2) during transcription elongation through the Mediator complex, while also phosphorylating key substrates involved in chromatin organisation and mRNA processing [5].

Over the past two decades, developments in cancer biology have underscored the importance of multi-omics approaches for elucidating kinase functions and identifying promising therapeutic targets. In particular, phosphoproteomics enables the direct detection of kinase substrates and their proximal neighbors, often uncovering unexpected cellular targets that can shed light on downstream signaling pathways [7]. For CDK8, which functions within the Mediator complex but may also act on a wider range of substrates involved in chromatin and RNA processing, phosphoproteomic profiling can help determine which cellular processes are directly influenced by CDK8 kinase activity versus those affected indirectly through changes in transcription [8, 9]. Additionally, time-resolved multi-omics techniques, sampling cells at different times after treatment, shed light on the sequence of molecular events, allowing us to differentiate early effects dependent on kinase activity from later responses driven by transcriptional changes [10].

Beyond identifying direct substrates, a complementary approach to understanding CDK8 function involves systematic mapping of its protein-protein interaction (PPI) networks. The Mediator complex is composed of more than 30 subunits organised into distinct functional modules, and CDK8 operates within a densely connected subnetwork that includes cofactors, RNA-processing machinery, and chromatin regulators, including BET proteins [11]. BET proteins, particularly BRD2, BRD3, and BRD4, have emerged as central hubs in the transcriptional control of cancer cells, acting as "readers" of acetylated chromatin through their bromodomains [12]. Of them, BRD4 facilitates the recruitment of the positive

transcription elongation factor complex (P-TEFb), which contains CDK9 and Cyclin T, to acetylated super-enhancers that govern oncogenic transcription factors such as MYC and BCL2 [13]. BET inhibitors, which competitively displace BET proteins from acetylated chromatin, have demonstrated preclinical and clinical activity across multiple cancer types and are currently being evaluated in early-phase AML trials [14]. In AML, both CDK8 and BET proteins converge on enhancer-driven transcriptional programs by integrating acetylation-dependent chromatin recruitment with Mediator-mediated signal-responsive transcriptional amplification, thereby controlling oncogenic and lineage-specific gene expression [15].

Our previous work has established that selective CDK8/CDK19 inhibition with RVU120 (Romaciclib; SEL120-34A) suppresses the growth of AML cell lines with LSC characteristics, including those expressing high levels of CD34 and elevated Ser726 phosphorylation of STAT5 (pSTAT5) [6]. Currently, RVU120 is being tested as monotherapy in stage II clinical trials for Myelodysplastic Syndrome (MDS) and myelofibrosis, as well as in combination with JAK inhibitors and venetoclax for myelofibrosis and Relapsed/Refractory (R/R) AML, respectively. Despite these advances, key questions persist regarding the temporal dynamics of CDK8 inhibitors' effects on LSC transcriptional networks and their synergy with conventional therapies. Recent work demonstrates that RVU120 synergises with venetoclax, hinting at combinatorial potential [16]. However, it remains unresolved whether RVU120’s anti-LSC activity derives from direct STAT5 inhibition or broader disruption of Mediator or other chromatin-associated complexes.

To further understand the molecular effects of CDK8 inhibition in LSCs, we undertook an integrated experimental approach combining multi-omics profiling, proteomic CDK8 interactome mapping, functional assays, and pharmacologic combination studies. Using TEX cells, an LSC-like model, we investigated the effects of CDK8 inhibition with two structurally distinct CDK8 inhibitors, RVU120 and CCT251921, on LSC properties, transcriptional and epigenetic programs, and PPIs. Our specific objectives were: (i) to confirm that CDK8 inhibition rapidly suppresses STAT5 phosphorylation and triggers differentiation in LSC-like cells; (ii) to employ integrated multi-omics analyses to define the temporal sequence and molecular coherence of CDK8-dependent transcriptional reprogramming; (iii) to perform survey of the CDK8 interactome and identify high-confidence, conserved interactors across multiple AML models; (iv) to identify the most abundant and druggable CDK8 interacting proteins suitable for combination therapy, and (v) to evaluate the translational potential of combinational CDK8 inhibition using multiple AML cell lines and patient-derived xenograft (PDX) models. Collectively, our experimental results, addressing the above objectives, position CDK8 as a central regulatory node in LSC maintenance and define a rational combination therapy approach for a clinically actionable subset of AML patients.

Materials and Methods

Chemicals

RVU120, CCT251921 and Pelabresib were provided by Ryvu. CB6644 was purchased from Merck. (SML3892) All chemical compounds were dissolved in Dimethyl Sulfoxide (DMSO) to prepare a 10 mM

stock solution and were stored at -80 ^{O}C.

Cell Culture

All leukemia cell lines were obtained from the American Type Culture Collection (Rockville, MD, USA). TEX cells were a generous gift from Dr. John Dick and provided under the MTA with University Health Network (Toronto, Canada). Cell lines were cultured in a humidified atmosphere containing 5% CO_2 at 37°C. TEX cells were maintained in their recommended media: IMDM (Gibco 21980-032) supplemented with 15% FBS (Gibco A5256701), 1 mM sodium pyruvate (Gibco 11360039), 1:100 Penicillin/Streptomycin (Gibco 15140122), 20 ng/ml SCF (R&D Systems 255-SC-050 or PeproTech 300-07), and 2 ng/ml IL-3 (R&D Systems 203-IL or PeproTech 200-03). MOLM-13, MOLM-14, MV4-11, and MOLM-16 cells were cultured in RPMI-1640 medium supplemented with 20% fetal bovine serum. KG-1 cells were cultured in IMDM medium supplemented with 10–15% FBS, 20 ng/ml SCF, and 2 ng/ml IL-3 (PeproTech, Cranbury, NJ, USA). Cells were harvested 1–2 times per week and reseeded at 4 × 10^5 cells/ml. All cell lines were authenticated using short tandem repeat profiling, and the absence of mycoplasma contamination was confirmed by the MycoAlert assay (Lonza LT07-518).

AML PDX development,

Patient-derived AML cells were obtained from the Institute of Hematology and Transfusion Medicine and the Military Institute of Medicine-National Research Institute. AMLX4 cells were purchased from Proxe (proxe.org). The cells were injected via the tail vein into 8-week-old female NSG-SGM3/J mice 24 hours after 2.25 Gy of whole-body irradiation. Following cells isolation from mouse bone marrow, the engraftment of human CD45 cells was confirmed using FACS. The established PDXs AML cells were stored long-term in liquid nitrogen.

PDX-derived AML cells culture and treatment

PDX-derived AML cells were isolated from mouse bone marrow and cryopreserved long-term in liquid nitrogen. For in vitro experiments, frozen cells were thawed and allowed to recover for 24 hours in a specially enriched medium consisting of IMDM supplemented with BIT (15%), β-mercaptoethanol (0.1 mM), 1:100 Penicillin/Streptomycin, 1 mM sodium pyruvate, and a cytokine/inhibitor cocktail including SR1 (500 nM), UM729 (500 nM), SCF (100 ng/ml), G-CSF (20 ng/ml), FLT3-L (50 ng/ml), and IL-3 (20 ng/ml). After recovery, cells were maintained in suspension culture under standard conditions (37°C, 5% CO_2) and used for downstream synergy assays.

Flow Cytometry

TEX cells were seeded in the recommended media supplemented with EPO 2U/ml (Peprotech, 100 − 64) at a density of 1.2 x 10^6 cells/well in a 6-well plate and treated with 0,5 uM RVU120. Cells were re-

seeded every 3–4 days and analyzed by flow cytometry at day 4, 7, 11 and 14. TEX cells were incubated with Human Fc Block (BD 564220). Following blocking, samples were stained with an anti-human antibody panel containing and isotype controls: CD71 FITC (1:20, ImmunoTools 21810713), CD34 PE (1:20, BioLegend 343506), CD38 BV510 (1:20, BioLegend 356612), CD41 AF700 (1:80, Sony Biotech 2118640), mIgG1 FITC (200 ug/ul, BioLegend 400110), mIgG1 PE (200 ug/ul, BioLegend 400122), mIgG1 BV510 (100 ug/ul, BioLegend 400172), mIgG1 AF700 (500 ug/ul, Sony Biotech 2600720). Additionally, samples were stained with LIVE/DEAD Fixable Near-IR (Invitrogen L34976) to assess cell viability. Flow cytometry analysis was performed on the BD LSR Fortessa cytometer and using FlowJo software (v.10.8.1).

RNA isolation and sequencing

Total RNA was isolated from 1 million TEX cells using the DirectZol kit (Zymo Research). All samples were DNase-treated and eluted with 50 µl of water. The quality and quantity of isolated RNA were analysed using the 2100 Bioanalyzer System (Agilent 2100 Bioanalyzer Eukaryote Total RNA Nano Series II Kit). RNA-Seq as a Coding Transcriptome Sequencing (CTS) service was performed by CeGaT (≥ 1 µg of RNA with a concentration ≥ 40 ng/µl in at least 25 µl total volume).

RNA-Seq data processing

Demultiplexing of the sequencing reads was performed with Illumina bcl2fastq (2.20). Adapters were trimmed with Skewer (version 0.2.2) [17]. The quality of the FASTQ files was analysed with FastQC (version 0.11.5-cegat). The resulting fastq files were mapped to the reference genome (hg38) using the STAR aligner [18] version 2.7.10a with default parameters. The read assignments per gene were counted using htseq-count [19] (version 0.11.1), using default counting mode and reverse string assignment to genes.

Protein immunoprecipitation for WB

Tex cells (5 × 10^6 cells per sample) were resuspended in 1 mL of ice-cold IP buffer (150 mM NaCl, 50 mM Tris-HCl (pH 7.5), 5 mM EDTA (pH 8), 1% Triton X-100, 0.5% NP40, with protease and phosphatase inhibitors (Thermo Scientific, 78441). The cells were kept on ice for 5 minutes, then sonicated in aliquots (4 × 250 µL) using a Bioruptor Pico (Diagenode) at high intensity for 10 minutes. The lysates were clarified by centrifugation at 10,000 × g for 15 minutes at 4°C. To the cell lysates, 5 µg antibody was added: NFRKB (St John's Laboratory, STJ112163-100), NFRKB recombinant (Invitrogen, MA5-55502), NFRKB (Bethyl, A301-459A); BRD3 (Santa Cruz Biotechnology, sc-81202), CDK8 (Bethyl, A302-500A), gently resuspended by pipetting, and incubated overnight at a cold room (4°C) with rotation. To the cells (Ag)-Ab was added 50 µl Dynabeads (Invitrogen, 10001D) and incubated for 4h at RT with rotation. Afterwards, the tubes were placed on the magnet, and the supernatant (flow-through) was transferred to separate tubes. The samples (Ag-Dynabeads-Ab) were gently resuspended in 50 µl IP buffer, gently

resuspended by pipetting, and 12.5 µl 4x Laemmli Buffer (Bio Rad 1610747) was added, boiled (5 min 99°C). Samples were separated on the magnet, and the supernatant was transferred to a fresh tube. The samples were stored at -20°C.

Western blotting

Western blotting
Cells were lysed in a RIPA buffer (Thermo Scientific 89900) supplemented with phosphatase and protease inhibitors (Thermo Scientific 78444). The lysates were clarified by centrifugation and quantified using the Bradford assay (Sigma B6916). Equal amounts of whole-cell lysates were loaded on 4–15% tris-glycine gels (Bio-Rad 5678085), then transferred to PVDF membranes. Immunoblotting was performed using antibodies: NFRKB (1:1000 Bethyl A301-459A), BRD3 (1:1000 Santa Cruz Biotechnology, sc-81202), CDK8 (1:500 Santa Cruz Biotechnology, sc-1521), STAT5 (1:1000, CST 25656), p-STAT5a/b S726/731 (1:1000, Active Motif 39597), p-STAT5 Y694 (1:1000, CST 9359), Actin (1:8000, Sigma A2066), Vinculin (1:15000, Sigma V9131). Next, the membranes were washed with PBST buffer (4×) and incubated with appropriate HRP-conjugated secondary antibodies: goat anti-rabbit (Abcam, ab97051), goat anti-mouse (Abcam, ab6789) and donkey anti-goat (Abcam, ab97110). Proteins were visualised using the ChemiDoc MP Imaging System (Bio-Rad). Densitometry was performed using ImageLab software (v.5.1).

Proteins digestion

Cell pellets were reconstituted in a lysis buffer containing 20% trifluoroethanol (TFE), 10 mM tris(2-carboxyethyl)phosphine (TCEP), and 100 mM triethylammonium bicarbonate (TEAB). Lysis was performed by sonication in an ultrasonic bath for 30 minutes, followed by vortexing at 1000 rpm for 1 hour, and incubation at 60°C for 1 hour. Cysteine residues were blocked by incubating the samples with 30 mM S-methylmethanethiosulfonate (MMTS) for 10 min at room temperature. Before digestion, samples were diluted with 100 mM TEAB to reduce the TFE concentration to 8%. Proteolytic digestion was performed overnight at 37°C using 2 µg of trypsin (Promega GmbH, Mannheim, Germany). Following digestion, peptides were purified using 10 mg Oasis HLB columns (Waters). The cartridges were preconditioned with 1 ml of methanol and 1 ml of 0.1% formic acid (FA) in water. After sample loading and washing with 1 ml of 0.1% FA, peptides were eluted with 200 µl of 75% acetonitrile (ACN) and subsequently dried in a SpeedVac concentrator. The dried peptides were reconstituted in 100 mM TEAB, and their concentrations were determined using the Pierce™ Quantitative Colourimetric Peptide Assay (Thermo Fisher Scientific). Equal amounts of peptides were mixed to prepare an internal standard sample (IS) used for inter-TMT normalisation. 30 µg of peptides from each sample and IS in 92 µl of 100 mM TEAB were labelled with TMTpro 18plex (Thermo Fisher Scientific) tags in 40 µl acetonitrile for 1 hour on a vortex. The reaction was quenched by the addition of 8 µL 5% hydroxylamine. The labelling efficiency was checked (99.5% for all three sets) and samples were combined and desalted using four 30 mg Oasis HLB columns (Waters) per TMT set. Cartridges were preconditioned with methanol and 2%

ACN with 0.1% FA. After the sample was loaded and rinsed with 2% ACN and 0.1% FA, peptides were eluted from the columns with 400 µl 90% ACN and 0.1% FA. Aliquots were pulled and dried in a Speedvac.

Reversed-phase peptide fractionation at high pH

A total of 540 µg of peptides for each TMT set was reconstituted in 500 µl of 10 mM AH with 2% ACN. TMT-labelled peptides were fractionated using high-pH reverse-phase chromatography on an XBridge Peptide BEH C18 column (4.6 × 250 mm, 130 Å, 5 µm; Waters). Separation was performed at a flow rate of 0.8 ml/min over 64 min using a Waters Acquity UPLC H-Class system. The mobile phases consisted of water (A), ACN (B), and 100 mM AH (C), with phase C maintained at a constant 10% throughout the gradient. Fractions were collected every minute, starting from the fourth minute of the run. The following gradient was applied: 5–8% solvent B over 3 min, 8–15% over 9 min, 15–25% over 22 min, 25–33% over 10 min, 33–50% over 8 min, 50–90% over 6 min, followed by a 4 min isocratic hold at 90% B, and final column equilibration at 3% B for 2 min. Peptide elution was monitored at 214 nm. The collected 60 fractions were dried in a SpeedVac concentrator and reconstituted in Evosep solvent A (0.1% FA in water) by vortexing for 30 min, followed by sonication for 30 min. Fractions were concatenated by pooling every 30th fraction, yielding 30 samples per TMT set for LC-MS analysis. 2 µg of peptides from each concatenated fraction was loaded onto Evotips precolumns, as described in the LC-MS analysis section. The remaining sample from each TMT set was pooled, cleaned with 30 mg Oasis HLB columns, dried in a SpeedVac concentrator and subjected to phosphopeptide enrichment.

Phosphopeptide enrichment with Ti-IMAC

Phosphopeptide enrichment was performed using MagReSyn Ti-IMAC beads (Resyn Biosciences) following the manufacturer's protocol. Briefly, 480 µg of desalted TMT-labelled peptides per set was divided into two equal parts. Each portion was dissolved in 200 µl of Loading Buffer (0.1 M glycolic acid in 80% ACN and 5% TFA) and incubated with 50 µl of magnetic beads for 20 min at room temperature with gentle vortexing. After incubation, the supernatant was discarded, and the beads were washed with Wash Buffer to remove non-specifically bound peptides. Phosphopeptides were eluted sequentially with three additions of 100 µl 1% AH elution buffer containing 0%, 10%, and 20% ACN. The pulled eluates were dried in a SpeedVac concentrator and reconstituted in 50 µl of 0.1% FA.

Protein immunoprecipitation for Mass spectrometry

Preparation of Dynabeads A for Single IP Reaction. 50 µL of Dynabeads A (Invitrogen, 10001D) were placed on a magnet to separate them from the solution, and the supernatant was removed. The beads were washed 3 times with PBST (PBS with 0.02% Tween 20). 5 µg of the target antibody was added to the Dynabeads A (beads with IgG for background control and beads with the target antibody; unspecific rabbit IgG – Vector Labs, I-1000; 1 µg/µL or CDK8 - #A302-500A; Bethyl; 200 µg/mL). The beads with the antibody were incubated with rotation at room temperature for 30 minutes, then placed on the magnet, and the supernatant was removed. The beads were washed once by gentle pipetting with PBST. The crosslinking reaction was prepared with a 5 mM BS3 (Pierce, 21585) solution in CB (20 mM HEPES). The

antibody-coupled Dynabeads A were washed twice with 200 µL CB, placed on the magnet, and the supernatant was discarded. The antibody-coupled Dynabeads A were resuspended in 300 µL of 5 mM BS3 and incubated at room temperature for 30 minutes with tilting rotation. The crosslinking reaction was quenched by adding 15 µL of QB (1 M Tris-HCl, pH 7.5) and incubating at room temperature for 15 minutes with tilting rotation. The cross-linked antibody-coupled Dynabeads A were washed three times with 400 µL PBST.

Protein Immunoprecipitation from AML cell lines and PDX cell models. Cells pellets (5 × 10^6 cells per sample) were resuspended in 1 mL of ice-cold IP buffer (150 mM NaCl, 50 mM Tris-HCl (pH 7.5), 5 mM EDTA (pH 8), 1% Triton X-100, 0.5% NP40, with protease and phosphatase inhibitors). The cells were kept on ice for 5 minutes, then sonicated in aliquots (4 × 250 µL) using a Bioruptor Pico (Diagenode) at high intensity for 10 minutes. The lysates were clarified by centrifugation at 10,000 × g for 15 minutes at 4°C. Antibody-coupled Dynabeads A were washed once with IP buffer, placed on a magnet, and the supernatant was removed. The cell lysates were added to the IgG-Dynabeads A complex, gently resuspended by pipetting, and incubated for 30 minutes at 4°C with rotation. Afterwards, the tubes were placed on the magnet, and the supernatant (flow-through) was transferred to the CDK8-Dynabeads A complex, which was gently resuspended by pipetting and incubated for another 30 minutes at 4°C with rotation. The samples (Dynabeads-Ab-Ag) were placed on a magnet, washed 3 times with 200 µL of 150 mM Tris-HCl, pH 7.6, and then separated on the magnet. The Dynabeads-Ab-Ag complex was gently resuspended in 50 µL of 200 mM formic acid, placed on a magnet, and the supernatant was transferred to a fresh tube. The samples were stored at -80°C.

Mass spectrometry

Co-IP samples, as well as global fractions and phospho-enriched TMT samples, were analysed using an Evosep One (Evosep Biosystems) coupled to an Orbitrap Exploris 480 mass spectrometer (Thermo Fisher Scientific). Samples were loaded onto disposable Evotips C18 trap columns according to the manufacturer's instructions. One-third of each co-IP sample, or 20 µl of each TMT sample, was loaded. Evotips containing phosphopeptides were additionally washed four times with 3% ACN. Peptides were separated on an EV1106 analytical column (Dr Maisch C18 AQ, 1.9 µm, 150 µm ID, 15 cm; Evosep Biosystems). Global TMT samples were analysed at 500 nl/min using a 44 min gradient (30 samples per day), whereas phospho-enriched TMT and co-IP samples were analysed at 220 nl/min using an 88 min preformed gradient (15 samples per day). Data were acquired in positive ion mode using data-dependent acquisition. MS1 spectra were recorded at 60000 resolution with a normalised AGC target of 300% and automatic maximum injection time. The scan range was 300–1700 m/z for TMT samples and 300–1600 m/z for co-IP samples. For TMT samples, MS2 spectra were acquired at 30000 resolution with a standard normalised AGC target and automatic maximum injection time. The top 25 precursors were selected within a 1.2 m/z isolation window and analysed in TurboTMT mode ("TMTpro Reagents"). For co-IP samples, MS2 resolution was 15000, and the top 40 precursors were selected within a 1.6 m/z isolation window. Dynamic exclusion was set to 20 s (± 10 ppm), and the precursor intensity threshold was 5e3. A precursor fit threshold of 70% was applied to TMT samples. Precursors were fragmented by

HCD with a normalised collision energy of 30%. The spray voltage was 2.1 kV, the funnel RF level 40, and the heated capillary temperature 275°C.

Mass spectrometry data analysis

Offline recalibration and peptide and protein identification were performed using the MaxQuant/Andromeda software suite [20] (version 2.0.1.0) against the Homo sapiens SwissProt database (version 2022_03). The search included tryptic-generated peptides, with methylthio (C) set as a fixed modification and oxidation (M) as a variable modification. Phosphorylation (STY) was also selected as a variable modification for phosphoproteome analysis.

A reverse database was used for target/decoy-based statistical validation, with peptide and protein FDR set to 0.01. All peptides derived from common contaminant proteins were filtered from the results. Also, proteins with fewer than 2 unambiguously assigned peptides and those identified by peptides from other proteins were excluded from further analysis. Proteins matching the same set of peptides were clustered into metaproteins. MaxQuant results processing was performed in MScan, a software tool available at http://proteom.ibb.waw.pl/mscan.

Quantitative analysis of the whole-proteome and phosphoproteome of TEX cells included only proteins identified by at least two unique MS/MS-confirmed peptides in every TMT labelling repeat. Relative protein abundances were computed using reporter-ion MS2 quantification in MaxQuant and processed using the internal reference scaling (IRS) algorithm for labelling batch-effect elimination [21]. To minimise the influence of other non-biological sources of variation on the data, the log-transformed abundances were further normalised using a locally weighted regression smoother (LOESS) [22]. The results of co-immunoprecipitation experiments were analysed using a semi-quantitative spectral-counting approach and summarised using the APEX index [23].

Phosphoproteome quantitative analysis was based on unique peptides with a single phosphorylation site, identified by MS/MS and correctly quantified across all TMT labelling replicates. The threshold for MaxQuant's site-localisation probability was set to 0.90, and only the site with the highest probability was analysed for peptides with multiple potential modification localisations. The obtained site-specific quantitative values were referenced to appropriate protein abundances from the global analysis. [S/T]-P motif in the peptide sequence and kinases associated with phosphorylation sites were from the PhosphoSitePlus database [24], the study by Sugiyama et al. [25], and the iPTMNet database [26].

A resampling-based t-statistic test was used to identify differentially expressed proteins and phosphosites in pairwise comparisons. The resulting p-values were corrected for multiple hypothesis testing using the two-step Benjamini-Hochberg procedure to control the false discovery rate (FDR) [27]. The adjusted p-values and fold-change (FC) thresholds were set to 0.05 and 1.25, respectively. Unsupervised principal components analysis (PCA) was also used to evaluate the relationships among the studied samples. Statistical data analysis utilised the MATLAB-based MStat application (available at https://proteom.ibb.waw.pl/mstat).

Cut&Tag libraries preparation and sequencings

TEX cells were incubated in the presence of CDK8 kinase inhibitors (RVU120 or CCT251921 at 0.5 μM) and harvested after 24 h and 72 h. The Cut&Tag experiment was performed on 300,000 TEX cells per antibody, following the manufacturer's recommendations (CUT&Tag-IT™ Assay Kit, Active Motif, Catalogue No. 53165 or 53171). For the experiment, we used the following antibodies: H3K27ac (Active Motif, cat. no. 91193); H3K4me1 (Active Motif, cat. no. 39635); H3K4me3 (Active Motif, cat. no. 39060); RNAP2 CTD (Abcam, cat. no. Ab5095); MLL-4 (Millipore, cat. no. ABE1867); CDK8-500 (Bethyl, cat. no. A302-500); BRD3 (Invitrogen, cat. no. PA530263); NFRKB (Bethyl, cat. no. A301-459A). Prior to sequencing, all samples were adjusted to 10nM, mixed in equal amounts, and divided into two pools: pool 1 (S13662) and pool 2 (S13663). Library sequencing was performed using the paired-end 75 bp method on the NovaSeq 6000 instrument at CeGaT.

Cut&Tag data analyses

Raw sequencing reads were subjected to quality control and adapter trimming using Trimmomatic (version 0.39) [28]; with the parameters SLIDINGWINDOW:4:20 and MINLEN:20. High-quality reads were subsequently aligned to the Homo sapiens reference genome (GRCh38) using Bowtie2 [29] under default mapping conditions. Optical duplicates were identified and removed with the MarkDuplicates tool from the GATK package (version 4.2.3.0) [30], applying default settings except for *OPTICAL_DUPLICATE_PIXEL_DISTANCE* set to 12,000. Following duplicate removal, genome-wide coverage tracks were generated using bamCoverage [31] (version 3.5.1) with RPKM normalisation to enable comparison across samples. Enrichment peaks were identified using MACS2 [32] (version 2.2.7.1) with default peak-calling parameters, based on the GRCh38 reference genome assembly. Peaks were associated with genomics features with the ChIPpeakAnno package [33] (version 3.36.1). Functional annotation of differential peaks was conducted with ReactomePA package [34] (version 1.46.0). Binding profiles were prepared using DeepTools [31] (version 3.5.1).

High-content microscopy analyses and synergy testing

To analyse cell growth, the established AML cell lines (KG-1, MOLM-13 and MOLM-16) as well as PDX-derived AML lines (AMLX4, 12 and 53) grown in suspension were plated in 96-well culture plates in triplicates at 20,000 cells (established lines) or 40,000 cells (PDX-derived lines) per well in 160 μl of their culture medium. Cells were exposed to single or combined treatments with DMSO, CDK8 kinase inhibitors (RVU120 or CCT251921), BET inhibitor (pelabresib) or RUVBL1/2 complex inhibitor (CB6644). At the designated time points, the suspension cells were attached to μCLEAR® black 96-well plates (Greiner) precoated with Poly-D-Lysine (Gibco), then fixed with 4% formaldehyde and stained with Hoechst 33342 (10 μg/ml). For analysis of DNA replication MOLM-16 cells were treated with 10 μM EdU (Lumiprobe) for 1 hour prior to fixation. The incorporated EdU was detected by click chemistry staining with AF 488 azide (Lumiprobe) according to the manufacturer's instructions. In each case, the stained cells were imaged with the Opera Phenix (Revvity) high-content imaging system, at the IN-MOL-CELL facility of the International Institute of Molecular and Cell Biology in Warsaw (IIMCB), using a 10x

objective and confocal mode. Live cell counts were assessed based on the intensity, morphology and texture properties of Hoechst 33342-stained DNA, whereas the percentages of EdU-positive cells were calculated based on AF 488 azide staining intensity. All quantitative analyses were performed using the Harmony 4.9 software (Revvity). Functional interactions, such as additive or synergistic effects, between CDK8 inhibitors and pelabresib or CB6644 were analysed based on the results of live cell numbers using the Synergy Finder 3.0 tool [35].

Results

RVU120 Inhibits STAT5 Phosphorylation at S726 and Triggers LSC-like TEX Cell Line Differentiation.

We previously showed that the growth of AML cell lines with LSC characteristics, including $CD34^+$ surface antigens and increased pS726 STAT5, can be potently inhibited by RVU120 both in vitro and in vivo [6]. In this study, we used the TEX cell line as a LSC model for further functional studies. This line was derived from human $CD34^+$-enriched Linneg cord blood cells through an engineered disruption of differentiation and self-renewal due to expression of the TLS-ERG oncogene [36]. A time-course treatment of TEX cells with RVU120 resulted in a strong decrease in STAT5 Ser726/731 phosphorylation that was observed at 6h of treatment and remained throughout further time-points (Fig. 1A). Consistent with our findings in other cell lines, we observed that RVU120 impaired TEX cell growth in a dose-dependent and treatment time-dependent manner, with IC50 values decreasing from 0.261 to 0.039 between 7-day and 14-day treatments (Fig. 1B). To test whether TEX cell growth inhibition by RVU120 is due to cell cycle arrest or to induced cell death, we performed flow cytometry experiments. Analysing DNA replication by BrdU incorporation assay and total DNA content by DAPI staining, we observed that 3- or 6-day RVU120 treatment caused a modest increase in the percentage of cells in the G2/M phase, indicating a slight delay in mitotic progression (Additional file 1A; Fig. 1C). On the other hand, by staining cells with Annexin V and 7-AAD cell death markers, we observed a gradual increase in apoptosis between 7 and 14 days of treatment (Additional file 1B; Fig. 1D). Hence, we concluded that the effect of RVU120 on TEX cell growth was not due to cell cycle inhibition but rather to increased apoptotic death. RVU120 induced a gradual TEX cells differentiation. Treatment for 4 days led to a marked upregulation of CD38 expression, with more than 90% of cells exhibiting a $CD34^+/CD38^+$ committed myeloid progenitor phenotype (Fig. 1E). Prolonged exposure to RVU120 (up to 14 days) resulted in a loss of CD34 and CD38 progenitor markers and an increased expression of CD71 and CD41 in remaining cells, indicating further progression toward megakaryocytic/erythroid-like progenitors (Fig. 1E) [37]. Hence, targeting STAT5 phosphorylation in LSC-model TEX cells, using RVU120, coincided with suppression of the leukemic stem cell phenotype and commitment to myeloid differentiation. These results confirmed that the TEX cell line is a suitable model for functional studies of RVU120's mode of action on LSC cells.

CDK8 Inhibition Drives Time-Dependent Erythroid-like Differentiation Programs in TEX Cells Revealed by Integrated Multi-Omics Analyses.

To investigate the molecular effects of CDK8 inhibition on LSC-like cell line characteristics, we used two compounds with distinct pharmacophores: RVU120 and CCT251921. We conducted transcriptomic, proteomic, and phosphoproteomic analyses at 3, 24, and 72 hours post-treatment with each compound. Transcriptomic analyses identified 850/492, 2544/3956, and 3372/3361 differentially expressed genes (DEGs) at an adjusted p-value ≤ 0.05, respectively, for RVU120/CCT251921 at the indicated time points (Additional file 2; Fig. 2A). In addition, the survey revealed high consistency in the transcriptomic responses to both compounds, as reflected by sample clustering in Principal Component Analysis (PCA) and significant DEGs correlations of 0.82, 0.95, and 0.95 at the 3-, 24-, and 72-hour time points, respectively (Additional file 3). The DEGs identified by RNA-Seq for a given experimental condition were subsequently subjected to functional enrichment analyses with the Reactome database to elucidate the biological processes, molecular functions, and pathways associated with the observed transcriptional changes. The significant pathways were assigned only to overexpressed DEGs (Additional file 4). For both CDK8 inhibitors, the functional analysis showed potential early metabolic priming, with activation of cholesterol biosynthesis, followed by a steadily intensifying inflammatory program and, eventually, a commitment to the erythroid lineage state. This was exemplified by activation of the Erythropoietin Signalling pathway, including increased GATA1 gene expression, a master regulator of erythroid differentiation (Fig. 2B, C)

For whole-proteome and phosphoproteome analyses five biological replicates for each condition were prepared. The tryptic peptides were labeled with TMT reagents, and the samples were divided into portions either for a direct whole-proteome survey or phosphopeptide enrichment using Ti-IMAC beads. In the whole-proteome analysis, 6521 proteins, each with at least 2 peptides from MS/MS spectra (FDR ≤ 0.01) were identified. Only peptides with an unambiguous assignment to a single protein were considered (Additional file 5). Proteins with fully overlapping sets of peptides were “rolled up” into a single entry in the list. There were none, 40/43, and 446/481 differentially abundant proteins (FDR ≤ 0.05), respectively, at 3, 24, and 72 hours post-treatment with RVU120 / CCT251921 (Additional file 6). Of those, 32 and 428 were commonly altered at the 24- and 72-hour timepoints, respectively. The differentiating proteins at both time points were significantly correlated with their respective transcriptomic datasets, indicating that protein-level alterations largely mirror underlying gene expression changes in the system under study (Additional file 7). Among the set of shared differentially expressed proteins at the 72-hour time point, 249 were upregulated while 178 were downregulated. The functional analysis with the Reactome database of upregulated proteins, in addition to the activation of pathways observed in the transcriptome survey, revealed a significant overrepresentation of proteins belonging to extracellular matrix (ECM) proteins (FN1, COL2A1, HSPG2, THBS1), Integrins (ITGA2B, ITGA8, ITGAV, ITGB3) and cell adhesion molecules (ICAM1, ICAM2) (Additional file 8). The upregulation of these molecules is consistent with the proposed in vitro differentiation of TEX cells toward erythroid lineage, which involves recreating aspects of the erythroblastic island microenvironment to undergo proper differentiation [38].

In sum, our integrated multi-omics analyses, aligning with phenotypic observations, demonstrate that CDK8 inhibition via RVU120 or CCT251921 induces highly consistent, time-dependent changes at both

the transcriptomic and proteomic levels in the TEX cell line. These changes begin with early metabolic priming of cholesterol biosynthesis, followed by a pronounced inflammatory response and eventual erythroid commitment and differentiation.

Nucleic Acid-Binding Proteins are Enriched within the Phosphoproteome Following CDK8 Inhibition in The TEX Cell Line.

The impact of both CDK8 inhibitors on the TEX cell line phosphoproteome was assessed using the same samples as for the proteomic analysis, which were subsequently subjected to phosphopeptide enrichment, enabling direct normalisation of the direct site-specific quantitative values to the corresponding protein abundances from the global analysis. MaxQuant assigned sequences to 15,432 spectra, representing 6,680 peptides from 1,120 proteins (FDR ≤ 0.01); proteins with at least two peptides are considered reliably identified, and proteins with shared peptide lists were “rolled up” into a single entry in the list (Additional file 9). To narrow down the phosphosites to the most reliable ones, we applied stringent criteria. First, at least one peptide containing the specific site had to be confidently identified with an FDR ≤ 0.01, carry only one Phospho (STY) modification and exhibit correct quantitative values in each of the three TMT labelling replicates. Next, we required MaxQuant’s probabilistic modification site localisation score to be at least 0.90. Finally, when a peptide contained more than one possible modification site, the probability measure for the selected site had to be the highest among all potential sites to ensure accurate quantitative evaluation. These steps yielded 395 modification sites in 297 proteins, which were submitted for quantitative analysis (Additional file 10). There were none, 1/4, and 38/45 differentially abundant phosphopeptides (FDR ≤ 0.05), respectively, at 3, 24, and 72 hours post-treatment with RVU120 / CCT251921 (Additional file 11). One and 35 phosphosites were shared between the inhibitors, with concordant changes in abundance, and one and 11 exhibited CDK8 [S/T]-P-enriched motifs [8] at the 24- and 72-hour timepoints, respectively (Fig. 3A). To investigate functional relationships among proteins whose phosphorylation is altered by CDK8 inhibition, we analysed the shared set of 33 proteins at 72h using the STRING database. We found that this protein set forms a significantly interconnected network (PPI enrichment p-value: 1.17e-07), with an overrepresentation of nucleic acid-binding proteins (Fig. 3B). To relate the results of our phosphoproteomic analysis following CDK8 inhibition to other studies, we compared affected phosphopeptides with recent work by Chen et al. [9], who used the HEK293 cell line with CDK8/19 kinase domain mutations or Senexin B, a CDK8 inhibitor. We identified seven commonly affected phosphoepitopes concordant with the Chen et al. study, of which three: NUCKS1_S54, KHSRP_S274 and HNRNPA1_S6 were downregulated following 72h CDK8 inhibitor treatment in both studies, which suggests that these phosphoepitopes are CDK8 kinase phosphorylation substrates. Overall, phosphoproteomic profiling of TEX cells treated with CDK8 inhibitors identified 33 high-confidence phosphosites across 35 proteins, forming a network enriched for nucleic acid-binding proteins and including three phosphoepitopes that were concordantly downregulated with previously reported CDK8 substrates.

Proteomic Identification and Characterisation of the CDK8 Interactome in AML Models Designate Targets for CDK8 Inhibitor Combinatorial Therapy.

To identify CDK8 protein core interactors and determine if they change upon CDK8 inhibitors treatment, the TEX cell line was incubated with DMSO (control) or with RVU120 and CCT251921 for 3 hours, and five biological replicates per group were collected. We then used co-immunoprecipitation mass spectrometry (co-IP-MS) proteins identification, followed by label-free APEX semiquantitative analysis of CDK8 complex constituents. MaxQuant assigned sequences to 16,130 spectra, corresponding to 2,593 peptides (FDR ≤ 0.01), and identified 204 proteins by at least two peptides in at least three of the five biological replicates per group; all proteins present in IgG samples were excluded. (Additional file 12). For functional and semi-quantitative analyses, we identified 145, 177, and 168 proteins in control, RVU120-treated, and CCT251921-treated cells, respectively, with 125 core proteins common to all three conditions (Fig. 4A). 4, 25 and 14 protein were exclusively identified in control, RVU120 and CCT251921 treated cells, respectively, while 20 proteins were common for cells treated with both CDK8 inhibitors. To assign functional roles to the core CDK8-interacting proteins in the TEX cell line, we performed STRING analysis using the Reactome database. The CDK8 interactome was enriched for transcriptional regulatory complexes, with a predominant association with Mediator components and the RNAP2 transcription regulatory complex [11]. Beyond the transcriptional machinery, the interactome included members of the SWI/SNF chromatin-remodelling family, the INO80 complex, histone acetyltransferases (HATs), and multiple components of ribonucleoprotein complexes (Fig. 4B). Direct biochemical interactions have been reported between human SWI/SNF subunits (SMARCA4 and BAF47) and the Mediator subunits MED23 and MED26 [39]. Mediator also associates with HAT complexes; for example, in mice, the Ada-Two-A-containing HAT complex interacts with Mediator to regulate non-coding RNA genes [40]. The presence of RNA-binding proteins suggests broader connections between the CDK8 network and mRNA co-transcriptional processing. Consistent with this notion, a direct interaction between CDK8 and mRNA 3'-end processing factors was recently reported in HeLa cells [41]. Notably, our co-IP-MS analysis identified the mitochondrial pyruvate dehydrogenase complex, including DLAT, PDHB, DLST, and PDHA1. These mitochondrial proteins form 2-ketoacid dehydrogenase complexes and were recently shown to be recruited to Mediator to supply a local pool of acetyl-CoA for HATs [42]. Together, these data align with previous studies of the Mediator complex interactome, indicating that overrepresented PPIs within the CDK8 interactome in TEX cells involve the RNAP2-Mediator complex, chromatin remodelers (INO80, SWI/SNF), and regulatory proteins that control transcription, RNA processing, and chromatin structure. We next focused on the most abundant proteins in the CDK8 interactome, ranking them by the semi-quantitative APEX index, to identify CDK8 partners that could be targeted with available drugs in combination therapy. The top 20 most abundant proteins identified by the STRING analysis comprised three main nodes: Mediator complex components (MED4, MED20 and MED22), the INO80 complex (NRFKB, RUVBL1/2 and UCHL5) with the associated BRD3 protein, and RNA/DNA-binding proteins (Fig. 4C). The interaction of CDK8 with NFRKB and BRD3 was additionally confirmed in an independent co-IP reaction followed by Western blot (Additional file 13). To assess the relevance of CDK8 protein interactors in other AML models, we surveyed these interactors using co-IP-MS in three AML cell lines (MOLM13, MOLM16, and MV4-11) and two lines derived from AML PDX models (AMLX22 and AMLX73) (Additional file 14). The analysis identified 39 CDK8-interacting proteins across the tested models, of which 11, including IRF2BP2, RUVBL1/2, SFPQ, NUDT21, NELFA, NONO,

NFRKB, PABPC1, BRD3 and DPYSL20, were shared with the top 20 core CDK8 proteins identified in the TEX cell line. For further functional experiments, we designated the INO80 complex and BRD3, as these constituents already have available small-molecule inhibitors. Specifically, CB6644 is a selective, allosteric inhibitor of the INO80 complex RUVBL1/2 ATPases [43], whereas Pelabresib is a small-molecule BET inhibitor for the treatment of myelofibrosis [44]. In sum, the proteomic characterisation of the CDK8 interactome in several AML models defined a conserved core network of transcriptional and chromatin-remodelling factors, notably the INO80 complex and BRD3, thereby identifying these interactors as chromatin CDK8-associated partners and potential actionable targets for combinational AML therapy with CDK8 inhibitors, which was tested next.

Genomic Occupancy Profiling Reveals Distinct Chromatin Remodeling Programs Following CDK8 Inhibition.

To investigate the genomic occupancy of NFRKB and BRD3, both implicated in chromatin-mediated transcriptional control, we performed CUT&Tag assays in TEX cells. In parallel, we profiled CDK8, RNAP2, KMT2D/MLL4, and three histone modifications: H3K27ac and H3K4me1 (active enhancer markers), and H3K4me3 (an active promoter marker) at 24 and 72 hours following treatment with CDK8 inhibitors. Overall, we processed 8 factors across two time points and two CDK8 inhibitors in three biological replicates, yielding 108 CUT&Tag libraries. Because the transcriptomic responses to RVU120 and CCT251921 were highly similar, we merged their datasets for each protein or histone mark in pairwise comparisons with untreated cells (DMSO). The inspection of investigated factors binding around transcription start sites (TSSs) and transcription end sites (TESs) genome-wide illustrated a loss of CDK8 binding and a coordinated gain in signals for other factors following CDK8 inhibition (Fig. 5A). To functionally interpret genomic context for the observed binding changes, the occupancy peaks for each factor exhibiting differential abundance following CDK8 treatment (Additional file 15) were systematically annotated to established Cis-Regulatory Elements (cCREs) by the ENCODE Project Consortium [45], including promoters, CTCF-binding sites, and both proximal and distal enhancer regions. At promoter regions, the majority of factors displayed strong net gains in occupancy or signal intensity (Fig. 5B, upper panel). H3K27ac increased by > 6,000 peaks at 24 h and > 5,600 at 72 h, reflecting widespread activation. H3K4me3 showed balanced changes (4,023 up/2,818 down at 24 h; 4,483 up/2,088 down at 72 h), suggesting both new promoter activation and partial silencing of previously active sites. Analysis of the correlation patterns revealed a highly interconnected core network: RNAP2 exhibited very high temporal stability (r = 0.91) and strong correlations with H3K4me3, MLL4, CDK8, and NFRKB (ranging from 0.51 to 0.76) (Fig. 5B, lower panel). Despite an early decline in CDK8 peaks (234 down versus 81 up at 24 hours), the protein migrated to sites occupied by core transcriptional machinery, re-establishing a remodeled landscape by 72 hours (202 up versus 155 down). Enhancers showed significant remodelling, H3K27ac increased by approximately 4,000 proximal and over 7,000 distal peaks at both time points, with only minimal losses, indicating persistent acetylation. H3K4me1 accumulated at about 2,800 proximal and between 11,500 and 12,000 distal sites. Notably, H3K4me1 demonstrated high temporal correlation (r = 0.89) but very weak correlations with other factors (r = 0.13 to 0.42), including RNAP2 (r = 0.16 to 0.18), suggesting it marks a distinct class of distal

enhancers that undergo large-scale priming independently of immediate transcriptional activity. RNAP2 occupancy at enhancers increased markedly (940 proximal, 1,900 distal at 24 hours), suggesting increased eRNA production [46]. MLL4 and NFRKB showed strong gains at enhancers with high correlations within the core network (r = 0.58 to 0.76), yet their correlations with H3K4me1 were weak (r = 0.27 to 0.36), indicating they are preferentially recruited to promoter-proximal or RNAP2-engaged enhancers. BRD3 accumulated at hundreds of new promoters (308 at 24 hours, 270 at 72 hours) and enhancers with minimal losses, but its correlations with other factors were weakest (r = 0.15 to 0.49), including with H3K27ac (r = 0.26 to 0.30) and H3K4me1 (r = 0.15 to 0.20), despite being a known acetyl-lysine reader. This suggests that BRD3 binds selectively to a small subset of acetylated sites within specific chromatin environments. CTCF-associated peaks showed modest changes, suggesting that CDK8 inhibition remodels cis-regulatory elements within existing topological frameworks [47]. Over time, from 24 to 72 hours, a progressive stabilisation was observed. High correlations across the board, H3K4me1 (r = 0.89), H3K27ac (r = 0.8), RNAP2 (r = 0.91), MLL4 (r = 0.76), NFRKB (r = 0.76), and CDK8 (r = 0.67), indicate that although peak numbers fluctuate, the relative patterns of occupancy remain consistent, pointing to the consolidation of a new regulatory state.

A systematic evaluation of the Reactome pathway enrichment across datasets, covering all factors at 24- and 72-hour timepoints, revealed a landscape of biological processes (Fig. 5C, Additional file 16). While no single pathway reached statistical significance across all conditions, the analysis highlights two main regulatory programs: a primary proliferative and transcriptional axis common to most factors, and a distinct immune-signaling signature associated with the H3K4me1 enhancer mark. Most factors (except H3K4me1) showed enrichment for pathways involved in M phase, RNA processing, such as splicing and pre-mRNA processing, and chromatin remodeling, including histone acetyltransferases and chromatin-modifying enzymes. This suggests a coordinated regulation of the cell cycle and transcriptional machinery. Conversely, regions marked by H3K4me1 are specifically enriched for immune-related pathways, such as neutrophil degranulation, interleukin signaling, and Fc-gamma receptor-mediated phagocytosis. These results imply that while active transcription supports proliferative functions, the enhancer landscape maintains a separate immune surveillance program. Overall, CUT&Tag occupancy profiling shows that inhibiting CDK8 in TEX cells induces coordinated chromatin remodelling, characterised by widespread increases in activation marks such as H3K27ac, H3K4me1, and H3K4me3, and the presence of co-regulatory factors such as RNAP2, MLL4, NFRKB, and BRD3 at promoters and enhancers. Correlation analysis indicates stable core transcriptional networks with high persistence over time (r = 0.67–0.91), whereas H3K4me1 marks a distinct, functionally independent distal enhancer landscape. Pathway analysis highlights two key regulatory programs: one associated with proliferation and transcription at promoters, and another linked to immune signaling at H3K4me1-marked enhancers. In summary, these findings support the idea that CDK8 acts as a molecular brake on chromatin accessibility. Inhibiting it shifts the epigenetic landscape toward a more permissive, highly acetylated state organised into modules that promote coordinated differentiation programs.

Dual Inhibition of CDK8 and BET Bromodomains Synergistically Eradicates Leukemia Cells in some AML models.

To accurately assess whether inhibiting INO80 or BRD3-related processes could provide an advantage when combined with CDK8 inhibitors, we used a high-content screening (HCS) approach on an Opera HCS confocal microscope. We thereby measured the effects of single or combined treatments (for 3, 6, 9, or 12 days) on the growth and survival of three AML cell lines, KG-1, MOLM-16, and MOLM-13, which, as we previously reported, differ in sensitivity to CDK8 inhibition [6]. Consistent with our previous findings, using the HCS-based approach, we verified that among these cell lines, KG-1 is the most sensitive, MOLM-13 is the least sensitive, whereas MOLM-16 shows moderate sensitivity to RVU120 or CCT251921 treatment (Fig. 6A-B). Treatment with CB6644 alone, although it did not affect the growth of KG-1 cells, impaired the growth of MOLM-16 and MOLM-13 cells in a dose-dependent manner, with the strongest effect observed in MOLM-13 cells (Fig. 6A). Conversely, Pelabresib treatment alone did not markedly impair the growth of any of the three cell lines (Fig. 6B). In KG-1 or MOLM-13 cells, co-treatment with CB6644 or Pelabresib did not affect the responses to RVU120 or CCT251921 treatment (Fig. 6A-B). However, we discovered that combining each CDK8 inhibitor with CB6644 or Pelabresib led to strong impairment of MOLM-16 cell growth, observed after 6, 9, and 12 days of treatment with CB6644 (Fig. 6A) and at all timepoints, starting from 3 days, with Pelabresib (Fig. 6B). The observed rates of MOLM-16 cell growth inhibition upon single and combined treatments with CB6644 and CDK8 inhibitors indicated additive effects. Pelabresib, however, appeared to act synergistically with CDK8 inhibitors, as it did not impair cell growth alone but strongly potentiated the effects of RVU120 or CCT251921 (Fig. 6B).

To verify a potential synergy between CDK8 inhibitors and Pelabresib in affecting MOLM-16 cell growth, we treated these cells for three days with various concentrations of each drug, assessed cell growth using an HCS-based approach, and performed a synergy matrix analysis, in which synergistic effects are characterised by a Bliss score > 10. This analysis confirmed that in MOLM-16 cells, Pelabresib acts synergistically with both RVU120 (Bliss Score = 10.021) and CCT251921 (Bliss Score = 16.152; Fig. 6C).

To study in more detail the interplays between CDK8 inhibitors and CB6644 or Pelabresib in regulating cell growth and survival, we used HCS microscopy to assess the effects of single or combined treatments for 6 days on DNA content (measured by Hoechst dye staining) and DNA replication (measured by detecting incorporated EdU) of MOLM-16 cells. We observed that RVU120 and CCT251921, while having little effect on the number of cells replicating DNA, led to the appearance of numerous debris-containing dead-cell DNA (Fig. 6D-F). This observation was consistent with the above-described results, which showed that in TEX cells, RVU120 has no effect on the cell cycle but induces apoptosis (as shown in Fig. 1D). Conversely, CB6644 mainly inhibited DNA replication and did not cause an apparent cell death (Fig. 6D-E). However, the combination of CB6644 with CDK8 inhibitors led to both outcomes, hence inhibited DNA replication, as upon single CB6644 treatment, and cell death, slightly more extensive than upon single CDK8i treatment (Fig. 6D-E). Therefore, CDK8 inhibitors and CB6644 exerted distinct effects on cell growth and survival, which may explain the additive action observed in the

combined treatment. Compared with CB6644, Pelabresib had only a minor effect on DNA replication, which was not strongly augmented by combination with CDK8 inhibitors (Fig. 6D and F). However, at higher concentrations, Pelabresib led to the appearance of some dead-cell remnants and upon combined treatment, it strongly intensified the effect of RVU120 or CCT251921 on cell death (Fig. 6D), indicating synergy in killing MOLM-16 cells. To validate the translational relevance of the observed synergy between inhibiting CDK8 inhibitors and Pelabresib, we extended the HCS-based combination matrix analysis to patient-derived AML cells. To this end, we tested three lines from PDX models AMLX4, AMLX12 and AMLX53. In AMLX4 and AMLX53, we identified synergy between RVU120/CCT251921 and Pelabresib (Bliss Scores > + 10; Fig. 7A-B), whereas in AMLX12, we observed additive effects (Bliss Scores < + 10; Fig. 7C).

Collectively, we discovered that combined CDK8 and BET inhibition represents a promising therapeutic strategy in a specific, clinically relevant subset of AML cases, in which BET inhibition potentiates CDK8 inhibitor-induced cell death.

Discussion

This study presents a multi-dimensional molecular portrait of CDK8 inhibition in AML stem-like cells, integrating time-resolved transcriptomics, proteomics, phosphoproteomics, interactome mapping, and chromatin profiling to establish CDK8 as a central node in LSC identity maintenance. The two structurally distinct inhibitors, RVU120 and CCT251921, produced highly concordant responses across all molecular layers, providing strong confidence that the observed effects are on-target. CDK8 inhibition rapidly suppressed STAT5 Ser726 phosphorylation, dismantled the $CD34^+$ stem-cell phenotype, and drove cells along an erythromegakaryocytic differentiation. Systematic interactome mapping identified BRD3 and the INO80 complex as conserved CDK8 partners across five AML models, while CUT&Tag profiling uncovered a chromatin remodeling program with distinct proliferative and immune-regulatory modules. Critically, these mechanistic observations translated into a pharmacologically actionable finding: CDK8 and BET inhibition synergised to eliminate AML cells in a context-dependent but reproducible manner, as confirmed in PDX models.

STAT5 Suppression and Erythromegakaryocytic Commitment

The time course of STAT5 Ser726/731 dephosphorylation, detectable within 6 hours yet preceding phenotypic differentiation by days, establishes this event as an early and reliable pharmacodynamic marker of CDK8 target engagement, consistent with prior characterisation of RVU120 in $CD34^+$ AML cell lines [6]. Importantly, cell loss in TEX cells was due to apoptosis rather than cell cycle arrest, as observed in other LSC models treated with CDK8 inhibitors. The progressive replacement of the $CD34^+/CD38^-$ phenotype with $CD38^+$, $CD71^+$, and $CD41^+$ surface markers over 14 days mirrors a stepwise transition through the bipotent megakaryocytic-erythroid progenitor hierarchy, rather than indiscriminate lineage bias. This pattern mirrors findings with MK256 [48], a structurally unrelated CDK8 inhibitor that similarly

induced maturation in $CD34^+/CD38^-$ LSCs, reinforcing the view that erythromegakaryocytic commitment upon CDK8 inhibition is a reproducible, mechanism-driven outcome. The upregulation of GATA1, a master erythroid transcription factor, is mechanistically coherent in this context; prior work established that STAT5-induced erythroid differentiation in hematopoietic progenitors is directly dependent on GATA1 activity [49], placing GATA1 as a downstream effector linking STAT5 suppression to lineage commitment. Whether CDK8 suppresses GATA1 directly, through phosphorylation of GATA1-associated coactivators, or indirectly through STAT5 regulation is an important mechanistic question that targeted genetic rescue experiments can address.

Temporal Multi-Omics Coherence

The phased molecular response to CDK8 inhibition constitutes one of the more illuminating aspects of this work. The early activation of cholesterol biosynthesis at 3 hours likely reflects metabolic reprogramming that primes cells for differentiation. Interestingly, previous work in Drosophila and mammalian models revealed that CDK8 restrains SREBP-driven lipid and cholesterol synthesis by phosphorylating SREBP, promoting its ubiquitination and degradation, thereby lowering lipogenic and cholesterogenic gene expression [50, 51]. This CDK8-dependent phenomenon is therefore evolutionarily conserved, making further exploration in AML and other cancers particularly warranted, especially given the broad clinical usage of statins, well-established inhibitors of cholesterol biosynthesis. The subsequent inflammatory gene activation at 24 hours is broadly consistent with the established role of inflammatory cytokine signaling in directing hematopoietic differentiation [52, 53], and positions CDK8 as a suppressor of inflammatory programs in LSCs. At 72 hours, the proteome extended beyond matching transcriptional changes to reveal upregulation of extracellular matrix proteins (fibronectin, collagens), integrins (ITGA2B, ITGB3), and cell adhesion molecules, features that collectively reconstitute aspects of the erythroblastic island microenvironment, which is essential for terminal differentiation [54, 55]. The strong concordance between proteomic and transcriptomic datasets at both 24 and 72 hours indicates that CDK8 inhibition propagates reliably from transcriptional rewiring to stable protein-level changes, a degree of coherence not always observed with kinase inhibitors and one that is important for biomarker development.

Phosphoproteomics: Substrates vs. Secondary Effects

The phosphoproteomic analysis identified 33 high-confidence altered phosphosites at 72 hours, with no detectable changes at 3 hours, a temporal profile suggesting a largely transcription-dependent, rather than direct kinase-driven, mechanism for most sites. Nonetheless, the 11 phosphosites carrying CDK8 consensus [S/T]-P motifs, particularly the three (NUCKS1_S54, KHSRP_S274, HNRNPA1_S6) that are concordant with the Chen et al. study in HEK293 cells [9], provide strong candidate direct substrates. HNRNPA1 links CDK8 activity to alternative splicing and mRNA processing [56], while NUCKS1 is a chromatin-associated regulator enriched at active promoters [57], both connect CDK8 to post-transcriptional gene regulation alongside its canonical transcriptional functions. The enrichment of nucleic acid-binding proteins across the affected phosphoproteome broadly aligns with the recently

described direct interaction between CDK8 and mRNA 3'-end processing factors [41], extending this functional axis into the LSC context. The smaller phosphosite yield relative to cortistatin A-based study [8] most likely reflects the stringent localisation and quantification criteria applied here; identified candidates warrant orthogonal biochemical confirmation.

The CDK8–BRD3 Axis and Its Erythroid Dimension

The co-IP-MS data revealed a conserved CDK8 interaction network, encompassing Mediator components, the INO80 complex, and BRD3, across five AML models, nominating BRD3 as a physically proximate and functionally relevant CDK8 partner. BRD3 has been shown to bind acetylated GATA1 via its first bromodomain and co-occupy most GATA1 target loci genome-wide, with its recruitment largely independent of the histone acetylation state [58], a behavior that directly mirrors the CUT&Tag observation that BRD3 occupancy increases at hundreds of new promoters and enhancers upon CDK8 inhibition despite only weakly correlating with H3K27ac ($r \approx 0.26–0.30$). Taken together, these data suggest that BRD3 redistribution upon CDK8 inhibition could be driven by GATA1-dependent chromatin targeting, positioning BRD3 as both a molecular consequence of CDK8 inhibition and an amplifier of the erythroid differentiation program, a mechanistic connection not previously described in AML.

Enhancer Remodeling and Chromatin State

CDK8 inhibition triggered a broad, predominantly unidirectional gain in H3K27ac (> 7,000 new distal peaks) and H3K4me1 marks, with minimal losses, consistent with CDK8 acting as a molecular brake on chromatin accessibility [11]. The separation of the enhancer landscape into two functionally distinct modules is a novel observation with real biological significance: a tightly coupled RNAP2–MLL4–CDK8–NFRKB–H3K27ac axis enriched for proliferative and transcriptional programs, and a decoupled distal H3K4me1 immune-regulatory program enriched for neutrophil degranulation and interleukin signaling pathways. CDK8's partial redistribution, declining at 24 hours then recovering at 72 hours, suggests adaptive reoccupancy rather than sustained eviction, which may reflect homeostatic transcriptional feedback. The minimal changes at CTCF-binding sites indicate that CDK8 inhibition remodels cis-regulatory elements within pre-existing topological domains, providing reassurance that the observed epigenetic effects are focal rather than architecturally destabilising [59]. The immune-regulatory enhancer module may represent a latent inflammatory identity normally suppressed in LSCs and liberated by CDK8 inhibition [60], potentially contributing to altered immune evasion alongside differentiation induction, a dimension worth exploring in co-culture systems with immune effector cells.

CDK8–BET Synergy: Mechanisms and Clinical Relevance

The pharmacologic synergy between CDK8 inhibitors and Pelabresib in MOLM-16 cells (Bliss scores of 10.0 and 16.2 for RVU120 and CCT251921, respectively) and its reproduction in two of three PDX models constitutes the most clinically actionable finding of this study. The mechanistic separation between the two drug classes, CDK8 inhibitors driving apoptosis without substantially affecting DNA replication, while Pelabresib amplified cell death in sensitive contexts, points toward convergence on a cell death

threshold rather than simple antiproliferative additivity, which matters for therapeutic index. The additive, rather than synergistic, response in AMLX12 underscores the context-dependence of this interaction. Pelabresib is already clinically active in myelofibrosis as part of the MANIFEST-2 combination regimen [44], providing a practical, safety-characterised clinical platform on which a CDK8-combination study in AML could be built.

Limitations and future directions

Several limitations need to be recognised. The TEX cell line, while well-validated as an LSC surrogate, is an engineered system that may not fully capture the genetic and epigenetic heterogeneity of primary AML. Multi-omics profiling was predominantly conducted in this single model, and validation in primary patient specimens spanning different AML molecular subclasses is needed before generalising the transcriptional and chromatin findings. The phosphoproteomic analysis, despite its rigour, applied stringent site-localisation thresholds that trade sensitivity for specificity; candidate substrates should be orthogonally confirmed by targeted kinase assays. The CUT&Tag profiling is correlational by design, and causal relationships between specific chromatin events and transcriptional outputs require perturbation experiments, such as CRISPR ablation of BRD3 or NFRKB, combined with rescue transcriptomics. Regarding future directions, genome-wide CRISPR loss-of-function screening in synergy-sensitive versus insensitive PDX models would be the most efficient approach to identifying predictive molecular determinants of CDK8-BET co-sensitivity, potentially moving beyond pSTAT5 Ser726 as a single biomarker. Targeted depletion of BRD3 combined with CUT&Tag re-profiling in TEX and primary AML cells would directly test whether BRD3 redistribution is causally required for the observed enhancer remodeling. In vivo combination studies of RVU120 and Pelabresib in NSG-SGM3 mice engrafted with defined sensitive and insensitive PDX models are needed to establish the therapeutic window and scheduling rationale that would support early-phase clinical trial design. Collectively, these experiments would close the loop between the mechanistic observations presented here and a molecularly stratified precision medicine approach for a clinically relevant subset of AML patients.

Conclusions

This work shows that CDK8 regulates LSC-like programs and demonstrates that inhibiting it in an AML model resembling LSCs triggers a coordinated differentiation program. This process is characterised by widespread changes in epigenetic marks, gene expression, proteins, and phosphoproteins. Our omics studies reveal that these changes are driven by a split in the chromatin landscape into two functional areas: one that responds to transcriptional stress by maintaining the cell cycle, and another stable enhancer program that shifts transcriptional resources toward immune signaling and differentiation. At the same time, mapping the proteins that interact with CDK8 reveals a network involving Mediator, chromatin remodelers, histone acetyltransferases, and RNA-binding proteins. Among these, INO80 and BRD3 stand out as potential targets for combination therapy. The conserved CDK8–BRD3 axis, combined with the observation of synergistic cell killing upon dual CDK8/BET inhibition in cell lines and PDX models, provides a mechanistic rationale and a directly actionable therapeutic strategy, with near-term

translational relevance leveraging RVU120 as a selective CDK8 inhibitor now in early-phase MDS, myelofibrosis and R/R AML clinical trials.

Abbreviations

CAN Acetonitrile

AML Acute Myeloid Leukemia

APEX Absolute Protein Expression (semi-quantitative index)

BET Bromodomain and Extra-Terminal domain

cCRE Candidate Cis-Regulatory Element

Co-IP-MS Co-Immunoprecipitation Mass Spectrometry

CUT&Tag Cleavage Under Targets and Tagmentation

DEG Differentially Expressed Gene

DMSO Dimethyl Sulfoxide

EPO Erythropoietin

eRNA Enhancer RNA

FACS Fluorescence-Activated C**ell Sorting**

FBS Fetal Bovine Serum

FC Fold Change

FDR False Discovery Rate

GEO Gene Expression Omnibu**s**

HAT Histone Acetyltransferase

HCS High-Content Screening

LSC Leukemic Stem Cell

MDS Myelodysplastic Syndrom**e**

PCA Principal Component Ana**lysis**

PDX Patient-Derived Xenograft

PPI Protein–Protein Interaction

RNAP2 Polymerase II RNA

RPKM Reads Per Kilobase per Million mapped reads

TES Transcription End Site

Ti-IMAC Titanium-Immobilized Metal Affinity Chromatography

TMT Tandem Mass Tag

TSS Transcription Start Site

Declarations

Ethics approval and consent to participate

The study was conducted in accordance with the Declaration of Helsinki. The use of AML patients' blasts for PDX development was granted by the Ethical Committee of the Institute of Hematology and Transfusion Medicine (opinion 54/2019).

Consent to Participate declaration

Informed consent to participate in the study was obtained from all participants.

All animal procedures were performed after the approval of the 2nd Local Ethics Committee for Animal Experimentation in Warsaw (permit WAW2/132/2022) and in compliance with to the European Parliament and the Council Directive (2010/63/EU) and the Polish regulations on the protection of animals used for scientific and educational purposes (Journal of Laws 2021, items 1331 and 2338).

Consent for publication

Not applicable

Availability of data and materials

The RNA-Seq data are available in the Gene Expression Omnibus (GEO) under the accession GSE309991. (token allowing review dataset: ifmdayoudbgrdkn)

The CUT&Tag data are available in the GEO under the accession GSE319092. (token: ypetamughhybzyl)

The MS data have been deposited to the ProteomeXchange Consortium via the PRIDE [61] partner repository with the dataset identifier PXD074404 and 10.6019/PXD074404. (token: rTIE7gluCKHG)

Competing interests

U.P., M.O., T.Rz. and M.Ma. are current or former Ryvu Therapeutics employees and/or shareholders. The remaining authors declare no competing interests.

Funding

The study was supported by the National Science Center grant (2018/30/E/NZ2/00801) (to M. Mi.).

Mass spectrometry software development was funded by Warsaw University of Technology within the Excellence Initiative: Research University (IDUB) programme (to T.Ru.).

Authors' contributions

M.Mi., T.Rz. and M.Ma. were responsible for conceptualisation, methodology, and investigation; M.S., I.R., U.P., M.O., M.K., J.C., M.C-L., E.K., Z.S-M., W.S-K., K.G., T.Ru., M.B., B.S. and A.P. performed experiments and/or analysed the data; K.K., P.R., J.K., K.K-W, P.J., T.Ru., M.B., B.S., A.P. and J.O. provided resources and/or guidance on experimental design; M.S., I.R., U.P., J.C.,T.Ru., M.B., B.S. and M.Mi. prepared the original manuscript draft; All authors reviewed and edited the manuscript; M.Mi, T.Rz., and M.Ma. supervised the study; and all authors have read and agreed to the published version of the manuscript.

Acknowledgements

Not applicable

References

1. Bonnet D, Dick JE. Human acute myeloid leukemia is organized as a hierarchy that originates from a primitive hematopoietic cell. Nat Med. 1997;3:730–7. https://doi.org/10.1038/nm0797-730.
2. Khaldoyanidi SK, Hindoyan A, Stein A, Subklewe M. Leukemic stem cells as a target for eliminating acute myeloid leukemia: Gaps in translational research. Crit Rev Oncol Hematol. 2022;175:103710. https://doi.org/10.1016/j.critrevonc.2022.103710.
3. Tam WF, Hähnel PS, Schüler A, Lee BH, Okabe R, Zhu N, et al. STAT5 is crucial to maintain leukemic stem cells in acute myelogenous leukemias induced by MOZ-TIF2. Cancer Res. 2013;73:373–84. https://doi.org/10.1158/0008-5472.CAN-12-0255.
4. Döhner H, Weisdorf DJ, Bloomfield CD. Acute Myeloid Leukemia. Longo DL, editor. N Engl J Med. 2015;373:1136–52. https://doi.org/10.1056/NEJMra1406184
5. Rzymski T, Mikula M, Wiklik K, Brzózka K. CDK8 kinase–An emerging target in targeted cancer therapy. Biochim Biophys Acta. 2015;1854:1617–29. https://doi.org/10.1016/j.bbapap.2015.05.011.

6. Rzymski T, Mikula M, Żyłkiewicz E, Dreas A, Wiklik K, Gołas A, et al. SEL120-34A is a novel CDK8 inhibitor active in AML cells with high levels of serine phosphorylation of STAT1 and STAT5 transactivation domains. Oncotarget. 2017;8:33779–95. https://doi.org/10.18632/oncotarget.16810.
7. de Oliveira PSL, Ferraz FAN, Pena DA, Pramio DT, Morais FA, Schechtman D. Revisiting protein kinase-substrate interactions: Toward therapeutic development. Sci Signal. 2016;9:re3. https://doi.org/10.1126/scisignal.aad4016.
8. Poss ZC, Ebmeier CC, Odell AT, Tangpeerachaikul A, Lee T, Pelish HE, et al. Identification of Mediator Kinase Substrates in Human Cells using Cortistatin A and Quantitative Phosphoproteomics. Cell Rep. 2016;15:436–50. https://doi.org/10.1016/j.celrep.2016.03.030.
9. Chen M, Li J, Zhang L, Wang L, Cheng C, Ji H, et al. CDK8 and CDK19: positive regulators of signal-induced transcription and negative regulators of Mediator complex proteins. Nucleic Acids Res. 2023;51:7288–313. https://doi.org/10.1093/nar/gkad538.
10. Turewicz M, Skagen C, Hartwig S, Majda S, Thedinga K, Herwig R, et al. Temporal phosphoproteomics reveals circuitry of phased propagation in insulin signaling. Nat Commun. 2025;16:1570. https://doi.org/10.1038/s41467-025-56335-6.
11. Richter WF, Nayak S, Iwasa J, Taatjes DJ. The Mediator complex as a master regulator of transcription by RNA polymerase II. Nat Rev Mol Cell Biol. 2022;23:732–49. https://doi.org/10.1038/s41580-022-00498-3.
12. Muddassir M, Soni K, Sangani CB, Alarifi A, Afzal M, Abduh NAY, et al. Bromodomain and BET family proteins as epigenetic targets in cancer therapy: their degradation, present drugs, and possible PROTACs. RSC Adv. 2020;11:612–36. https://doi.org/10.1039/d0ra07971e.
13. Lovén J, Hoke HA, Lin CY, Lau A, Orlando DA, Vakoc CR, et al. Selective inhibition of tumor oncogenes by disruption of super-enhancers. Cell. 2013;153:320–34. https://doi.org/10.1016/j.cell.2013.03.036.
14. Shorstova T, Foulkes WD, Witcher M. Achieving clinical success with BET inhibitors as anti-cancer agents. Br J Cancer. 2021;124:1478–90. https://doi.org/10.1038/s41416-021-01321-0.
15. Pelish HE, Liau BB, Nitulescu II, Tangpeerachaikul A, Poss ZC, Da Silva DH, et al. Mediator kinase inhibition further activates super-enhancer-associated genes in AML. Nature. 2015;526:273–6. https://doi.org/10.1038/nature14904.
16. Pakulska U, Obacz M, Woźnicki J, Wiklik K, Chakraborty S, Micek M, et al. Romaciclib, a CDK8/CDK19 inhibitor, can overcome venetoclax resistance through a combinatorial strategy. BioRxiv Prepr Serv Biol. 2026. https://doi.org/10.64898/2025.12.16.693978. 2025.12.16.693978.
17. Jiang H, Lei R, Ding S-W, Zhu S. Skewer: a fast and accurate adapter trimmer for next-generation sequencing paired-end reads. BMC Bioinformatics. 2014;15:182. https://doi.org/10.1186/1471-2105-15-182.
18. Dobin A, Davis CA, Schlesinger F, Drenkow J, Zaleski C, Jha S, et al. STAR: ultrafast universal RNA-seq aligner. Bioinf Oxf Engl. 2013;29:15–21. https://doi.org/10.1093/bioinformatics/bts635.

19. Anders S, Pyl PT, Huber W. HTSeq–a Python framework to work with high-throughput sequencing data. Bioinf Oxf Engl. 2015;31:166–9. https://doi.org/10.1093/bioinformatics/btu638.
20. Tyanova S, Temu T, Cox J. The MaxQuant computational platform for mass spectrometry-based shotgun proteomics. Nat Protoc. 2016;11:2301–19. https://doi.org/10.1038/nprot.2016.136.
21. Plubell DL, Wilmarth PA, Zhao Y, Fenton AM, Minnier J, Reddy AP, et al. Extended Multiplexing of Tandem Mass Tags (TMT) Labeling Reveals Age and High Fat Diet Specific Proteome Changes in Mouse Epididymal Adipose Tissue. Mol Cell Proteom MCP. 2017;16:873–90. https://doi.org/10.1074/mcp.M116.065524.
22. Bolstad BM, Irizarry RA, Astrand M, Speed TP. Bioinf Oxf Engl. 2003;19:185–93. https://doi.org/10.1093/bioinformatics/19.2.185. A comparison of normalization methods for high density oligonucleotide array data based on variance and bias.
23. Braisted JC, Kuntumalla S, Vogel C, Marcotte EM, Rodrigues AR, Wang R, et al. The APEX Quantitative Proteomics Tool: generating protein quantitation estimates from LC-MS/MS proteomics results. BMC Bioinformatics. 2008;9:529. https://doi.org/10.1186/1471-2105-9-529.
24. Hornbeck PV, Zhang B, Murray B, Kornhauser JM, Latham V, Skrzypek E. PhosphoSitePlus, 2014: mutations, PTMs and recalibrations. Nucleic Acids Res. 2015;43:D512–520. https://doi.org/10.1093/nar/gku1267.
25. Sugiyama N, Imamura H, Ishihama Y. Large-scale Discovery of Substrates of the Human Kinome. Sci Rep. 2019;9:10503. https://doi.org/10.1038/s41598-019-46385-4.
26. Huang H, Arighi CN, Ross KE, Ren J, Li G, Chen S-C, et al. iPTMnet: an integrated resource for protein post-translational modification network discovery. Nucleic Acids Res. 2018;46:D542–50. https://doi.org/10.1093/nar/gkx1104.
27. Benjamini Y, Hochberg Y. Controlling the False Discovery Rate: A Practical and Powerful Approach to Multiple Testing. J R Stat Soc Ser B Methodol. 1995;57:289–300. https://doi.org/10.1111/j.2517-6161.1995.tb02031.x.
28. Bolger AM, Lohse M, Usadel B. Trimmomatic: a flexible trimmer for Illumina sequence data. Bioinf Oxf Engl. 2014;30:2114–20. https://doi.org/10.1093/bioinformatics/btu170.
29. Langmead B, Salzberg SL. Fast gapped-read alignment with Bowtie 2. Nat Methods. 2012;9:357–9. https://doi.org/10.1038/nmeth.1923.
30. McKenna A, Hanna M, Banks E, Sivachenko A, Cibulskis K, Kernytsky A, et al. The Genome Analysis Toolkit: a MapReduce framework for analyzing next-generation DNA sequencing data. Genome Res. 2010;20:1297–303. https://doi.org/10.1101/gr.107524.110.
31. Ramírez F, Ryan DP, Grüning B, Bhardwaj V, Kilpert F, Richter AS, et al. deepTools2: a next generation web server for deep-sequencing data analysis. Nucleic Acids Res. 2016;44:W160–165. https://doi.org/10.1093/nar/gkw257.
32. Zhang Y, Liu T, Meyer CA, Eeckhoute J, Johnson DS, Bernstein BE, et al. Model-based analysis of ChIP-Seq (MACS). Genome Biol. 2008;9:R137. https://doi.org/10.1186/gb-2008-9-9-r137.

33. Zhu LJ, Gazin C, Lawson ND, Pagès H, Lin SM, Lapointe DS, et al. ChIPpeakAnno: a Bioconductor package to annotate ChIP-seq and ChIP-chip data. BMC Bioinformatics. 2010;11:237. https://doi.org/10.1186/1471-2105-11-237.
34. Yu G, He Q-Y. ReactomePA: an R/Bioconductor package for reactome pathway analysis and visualization. Mol Biosyst Royal Soc Chem. 2016;12:477–9. https://doi.org/10.1039/C5MB00663E.
35. Ianevski A, Giri AK, Aittokallio T. SynergyFinder 3.0: an interactive analysis and consensus interpretation of multi-drug synergies across multiple samples. Nucleic Acids Res. 2022;50:W739–43. https://doi.org/10.1093/nar/gkac382.
36. Warner JK, Wang JCY, Takenaka K, Doulatov S, McKenzie JL, Harrington L, et al. Direct evidence for cooperating genetic events in the leukemic transformation of normal human hematopoietic cells. Leukemia. 2005;19:1794–805. https://doi.org/10.1038/sj.leu.2403917.
37. Xavier-Ferrucio J, Krause DS. Concise Review: Bipotent Megakaryocytic-Erythroid Progenitors: Concepts and Controversies. Stem Cells Dayt Ohio. 2018;36:1138–45. https://doi.org/10.1002/stem.2834.
38. Ward CM, Ravid K. Matrix Mechanosensation in the Erythroid and Megakaryocytic Lineages. Cells. 2020;9:894. https://doi.org/10.3390/cells9040894.
39. Kowenz-Leutz E, Pless O, Dittmar G, Knoblich M, Leutz A. Crosstalk between C/EBPbeta phosphorylation, arginine methylation, and SWI/SNF/Mediator implies an indexing transcription factor code. EMBO J. 2010;29:1105–15. https://doi.org/10.1038/emboj.2010.3.
40. Krebs AR, Demmers J, Karmodiya K, Chang N-C, Chang AC, Tora L. ATAC and Mediator coactivators form a stable complex and regulate a set of non-coding RNA genes. EMBO Rep. 2010;11:541–7. https://doi.org/10.1038/embor.2010.75.
41. Lu C, Bai X, Zhang H, Zhang Y, Yang M, Zheng Y, et al. Mediator regulates transcriptional termination through crosstalk with pre-mRNA 3’ end processing factors. Mol Cell. 2025;85:2147–e216410. https://doi.org/10.1016/j.molcel.2025.05.006.
42. Russo M, Gualdrini F, Vallelonga V, Prosperini E, Noberini R, Pedretti S, et al. Acetyl-CoA production by Mediator-bound 2-ketoacid dehydrogenases boosts de novo histone acetylation and is regulated by nitric oxide. Mol Cell. 2024;84:967–e98010. https://doi.org/10.1016/j.molcel.2023.12.033.
43. Assimon VA, Tang Y, Vargas JD, Lee GJ, Wu ZY, Lou K, et al. CB-6644 Is a Selective Inhibitor of the RUVBL1/2 Complex with Anticancer Activity. ACS Chem Biol. 2019;14:236–44. https://doi.org/10.1021/acschembio.8b00904.
44. Ferreira Gomes G, Harrison C. Pelabresib (CPI-0610): An Exciting Novel Drug for the Treatment of Myelofibrosis. Curr Hematol Malig Rep. 2023;18:113–20. https://doi.org/10.1007/s11899-023-00696-6.
45. Moore JE, Pratt HE, Fan K, Phalke N, Fisher J, Elhajjajy SI, et al. An expanded registry of candidate cis-regulatory elements. Nat Nat Publishing Group. 2026;1–10. https://doi.org/10.1038/s41586-025-09909-9.

46. Li Q, Liu X, Wen J, Chen X, Xie B, Zhao Y. Enhancer RNAs: mechanisms in transcriptional regulation and functions in diseases. Cell Commun Signal CCS. 2023;21:191. https://doi.org/10.1186/s12964-023-01206-0.
47. Rinzema NJ, Sofiadis K, Tjalsma SJD, Verstegen MJAM, Oz Y, Valdes-Quezada C, et al. Building regulatory landscapes reveals that an enhancer can recruit cohesin to create contact domains, engage CTCF sites and activate distant genes. Nat Struct Mol Biol. 2022;29:563–74. https://doi.org/10.1038/s41594-022-00787-7.
48. Lee J-C, Liu S, Wang Y, Liang Y, Jablons DM. MK256 is a novel CDK8 inhibitor with potent antitumor activity in AML through downregulation of the STAT pathway. Oncotarget. 2022;13:1217–36. https://doi.org/10.18632/oncotarget.28305.
49. Caulier AL, Sankaran VG. Molecular and cellular mechanisms that regulate human erythropoiesis. Blood. 2022;139:2450–9. https://doi.org/10.1182/blood.2021011044.
50. Zhao X, Feng D, Wang Q, Abdulla A, Xie X-J, Zhou J, et al. Regulation of lipogenesis by cyclin-dependent kinase 8-mediated control of SREBP-1. J Clin Invest. 2012;122:2417–27. https://doi.org/10.1172/JCI61462.
51. Li X, Zhang M, Liu M, Liu T-H, Hemba-Waduge R-U-S, Ji J-Y. Cdk8 attenuates lipogenesis by inhibiting SREBP-dependent transcription in Drosophila. Dis Model Mech. 2022;15:dmm049650. https://doi.org/10.1242/dmm.049650.
52. Collins A, Mitchell CA, Passegué E. Inflammatory signaling regulates hematopoietic stem and progenitor cell development and homeostasis. J Exp Med. 2021;218:e20201545. https://doi.org/10.1084/jem.20201545.
53. Schippel N, Sharma S. Dynamics of human hematopoietic stem and progenitor cell differentiation to the erythroid lineage. Exp Hematol. 2023;123:1–17. https://doi.org/10.1016/j.exphem.2023.05.001.
54. Lazar-Karsten P, Dorn I, Meyer G, Lindner U, Driller B, Schlenke P. The influence of extracellular matrix proteins and mesenchymal stem cells on erythropoietic cell maturation. Vox Sang. 2011;101:65–76. https://doi.org/10.1111/j.1423-0410.2010.01453.x.
55. Elvarsdóttir EM, Mortera-Blanco T, Dimitriou M, Bouderlique T, Jansson M, Hofman IJF, et al. A three-dimensional in vitro model of erythropoiesis recapitulates erythroid failure in myelodysplastic syndromes. Leukemia. 2020;34:271–82. https://doi.org/10.1038/s41375-019-0532-7.
56. Sun Y, Xiong B, Shuai X, Li J, Wang C, Guo J, et al. Downregulation of HNRNPA1 induced neoantigen generation via regulating alternative splicing. Mol Med Camb Mass. 2024;30:85. https://doi.org/10.1186/s10020-024-00849-0.
57. Østvold AC, Grundt K, Wiese C. NUCKS1 is a highly modified, chromatin-associated protein involved in a diverse set of biological and pathophysiological processes. Biochem J. 2022;479:1205–20. https://doi.org/10.1042/BCJ20220075.
58. Lamonica JM, Deng W, Kadauke S, Campbell AE, Gamsjaeger R, Wang H, et al. Bromodomain protein Brd3 associates with acetylated GATA1 to promote its chromatin occupancy at erythroid target genes. Proc Natl Acad Sci U S A. 2011;108:E159–168. https://doi.org/10.1073/pnas.1102140108.

59. Dimitrova E, Feldmann A, van der Weide RH, Flach KD, Lastuvkova A, de Wit E, et al. Distinct roles for CKM-Mediator in controlling Polycomb-dependent chromosomal interactions and priming genes for induction. Nat Struct Mol Biol. 2022;29:1000–10. https://doi.org/10.1038/s41594-022-00840-5.
60. Ellegast JM, Alexe G, Hamze A, Lin S, Uckelmann HJ, Rauch PJ, et al. Unleashing Cell-Intrinsic Inflammation as a Strategy to Kill AML Blasts. Cancer Discov. 2022;12:1760–81. https://doi.org/10.1158/2159-8290.CD-21-0956.
61. Perez-Riverol Y, Bandla C, Kundu DJ, Kamatchinathan S, Bai J, Hewapathirana S, et al. The PRIDE database at 20 years: 2025 update. Nucleic Acids Res. 2025;53:D543–53. https://doi.org/10.1093/nar/gkae1011.

Figures

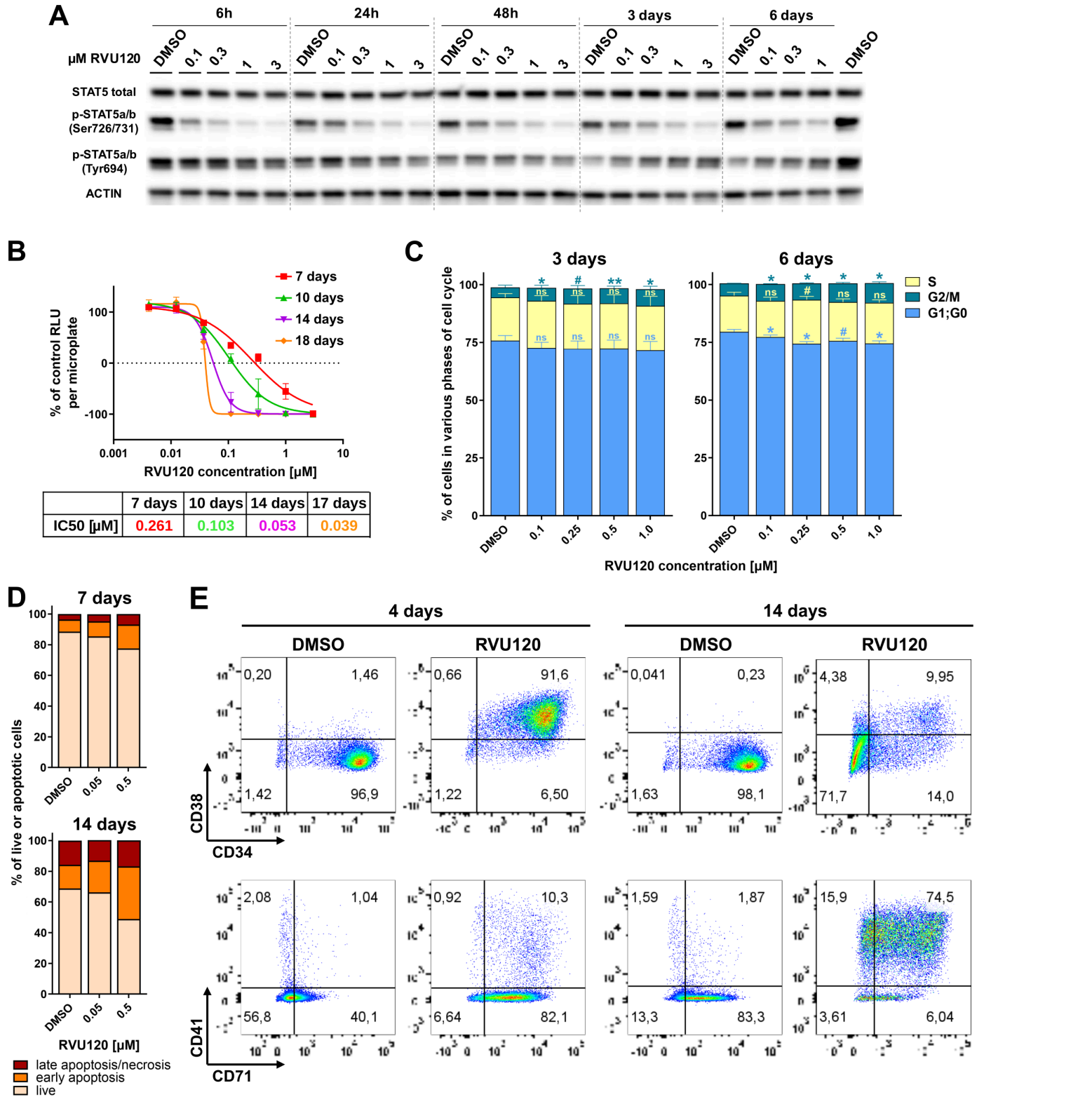

Figure 1

RVU120 inhibits STAT5 phosphorylation at S726 and triggers LSC-like TEX cell line differentiation. (A) STAT5 expression and p-STAT5 (S726/S731) / p-STAT5 (Y694) abundance evaluation in TEX cells treated with the indicated concentrations of RVU120 for 6, 24, 48, 72 and 144 hours. Actin and Vinculin were used as loading controls. Representative western blots are shown (n=2 and n=3 for 24, 72 and 144h). **(B)** Long-term viability of TEX cells treated with increasing concentrations of RVU120 for 7, 10, 14,

and 18 days. Data are mean ± SD of technical triplicates from a representative experiment (n= 3). A representative graph is shown. **(C)** Cell cycle analysis based on flow cytometric detection of incorporated BrdU and DAPI staining intensity in TEX cells treated for 3 or 6 days with DMSO or RVU120 at the indicated concentrations. Mean values (± SEM) of the cell percentage in each cell cycle phase (S, G2/M or G1;G0) compared statistically to the results for DMSO-treated cells (n= 3, for 3 days and n=4 for 6 days). The analysis includes the representative flow cytometry experiment shown in Additional file 1A. **(D)** Representative results of flow cytometric cell death assessment in TEX cells stained with Annexin V and 7-AAD after treatment with DMSO or RVU120 at indicated concentrations for 7 or 14 days. The graphs show the percentage of live, apoptotic or dead cells (n=1), which is also visualised in the flow cytometry scatter plots in Additional file 1B. **(E)** Representative Immunophenotyping of TEX cells treated with 0.5 μM RVU120 for 4 and 14 days. Scatter plots show the expression of surface markers: CD34, CD38, CD71 and CD41 at the indicated time points. P-values of statistical analysis in C are highlighted as: ns (P > 0.1), **#** (P < 0.1), * (P < 0.05) or ** (P < 0.01).

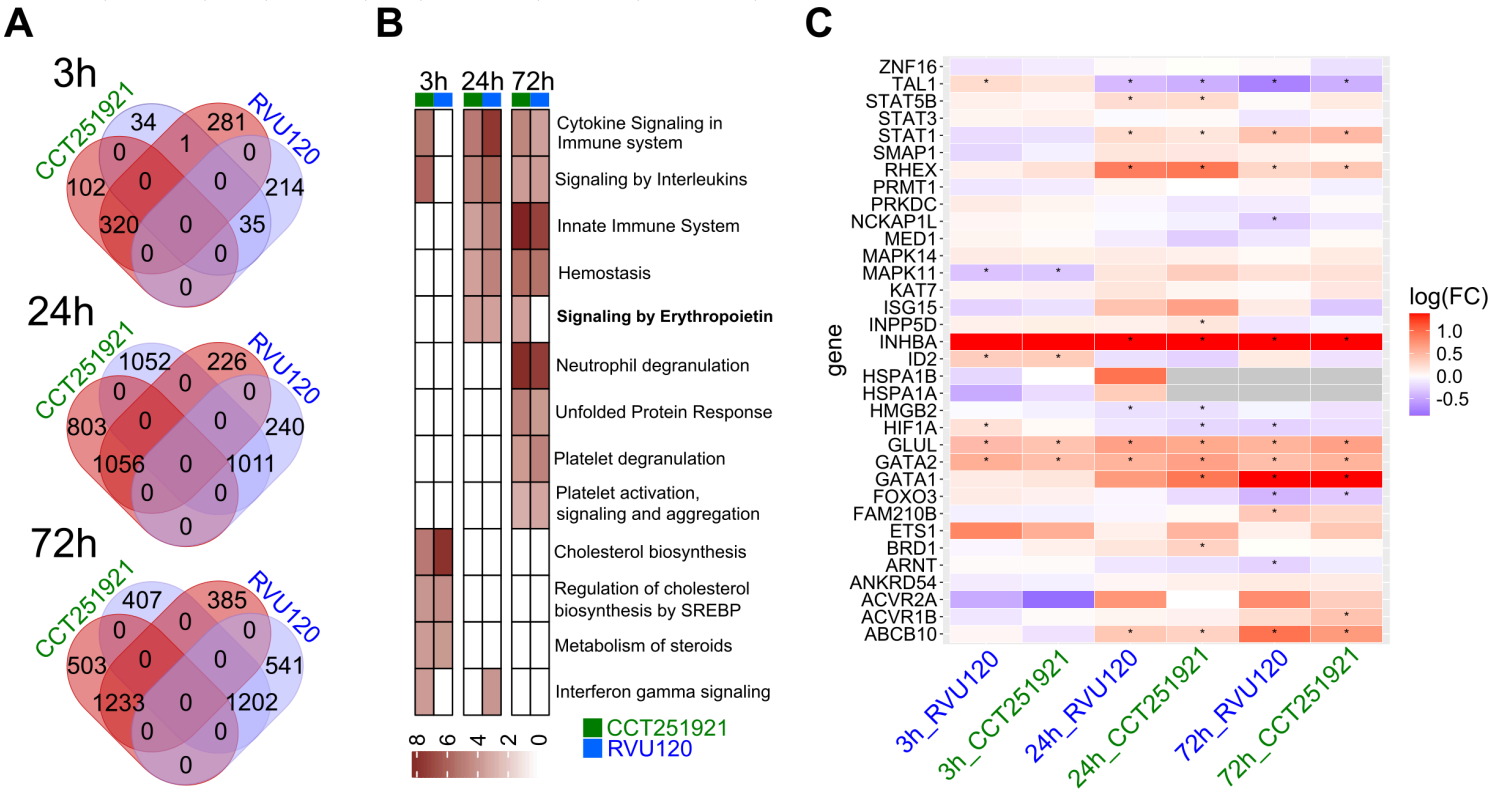

Figure 2

Transcriptomic profiling and functional changes in the TEX cell line following CDK8 inhibition. (A) Venn diagrams showing overlapping numbers of differentially expressed genes (DEGs) at 3h, 24h and 74h following the RVU120 and CCT251921 treatment in the TEX cell line. Red and blue shading denote up- and downregulated DEGs, respectively. **(B)** Significantly altered (adj. p-value < 0.05) recurrent Reactome terms for the upregulated DEGs after the RVU120 and CCT251921 treatment. The p-value is shown on the PHRED scale. **(C)** The expression heatmap with genes playing an important role in erythropoiesis. The expression values were extracted from the RNA-Seq dataset. DEGs with adj. P-values <0.05 are highlighted with an asterisk (*).

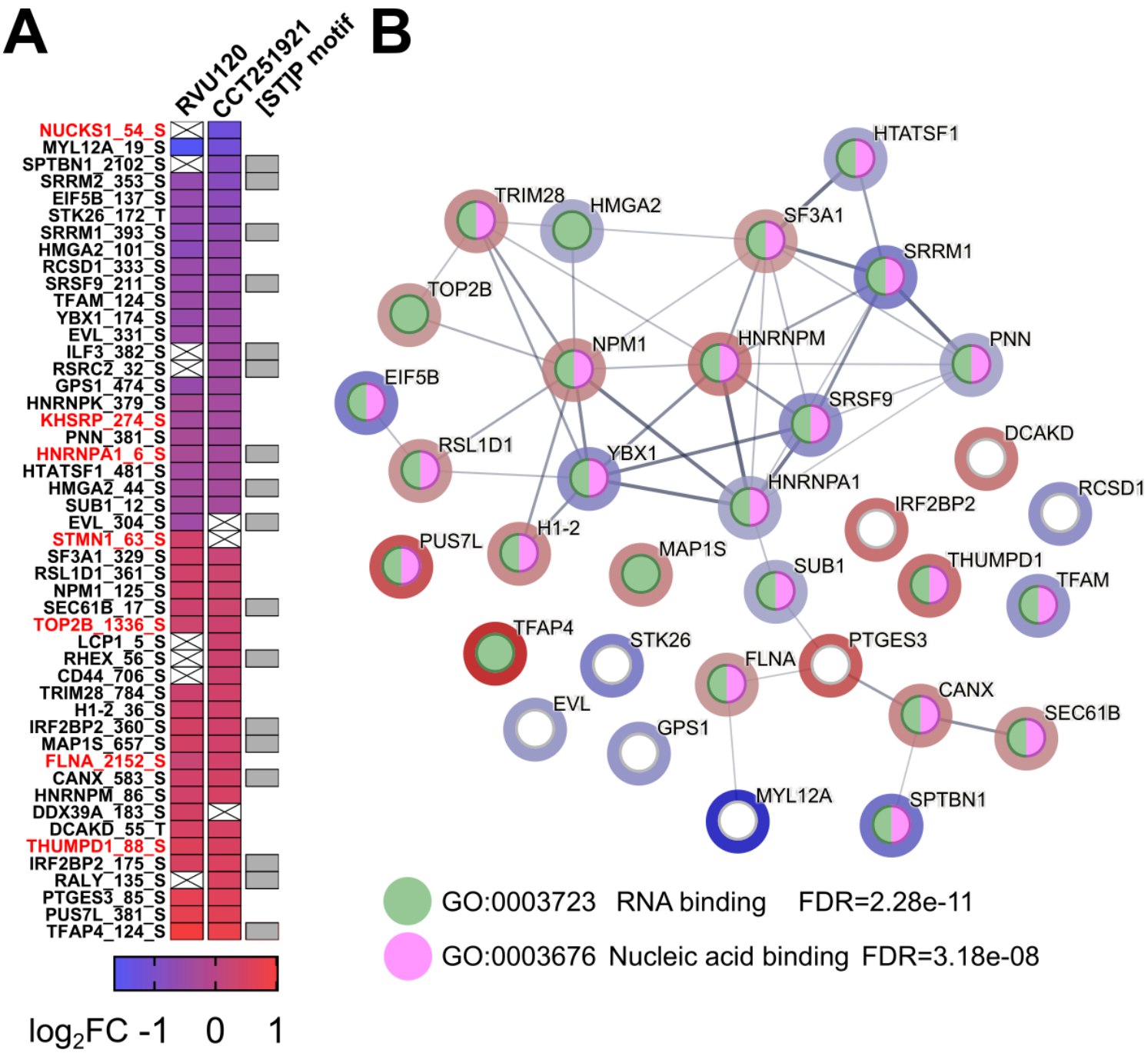

Figure 3

Nucleic acid-binding proteins are enriched in the phosphoproteome following CDK8 Inhibition in the TEX cell line. (A) Heatmap of significantly altered 33 phosphosites with concordant changes in abundance after 72h treatment with CDK8 inhibitors. In red, the phosphosites are those shared with the work by Chen et al. (8). **(B)** String analysis of network nodes of proteins with identified phosphosites, line thickness indicates the strength of data support. The halo colour indicates the phosphosite abundance after 72h of CDK8 inhibition.

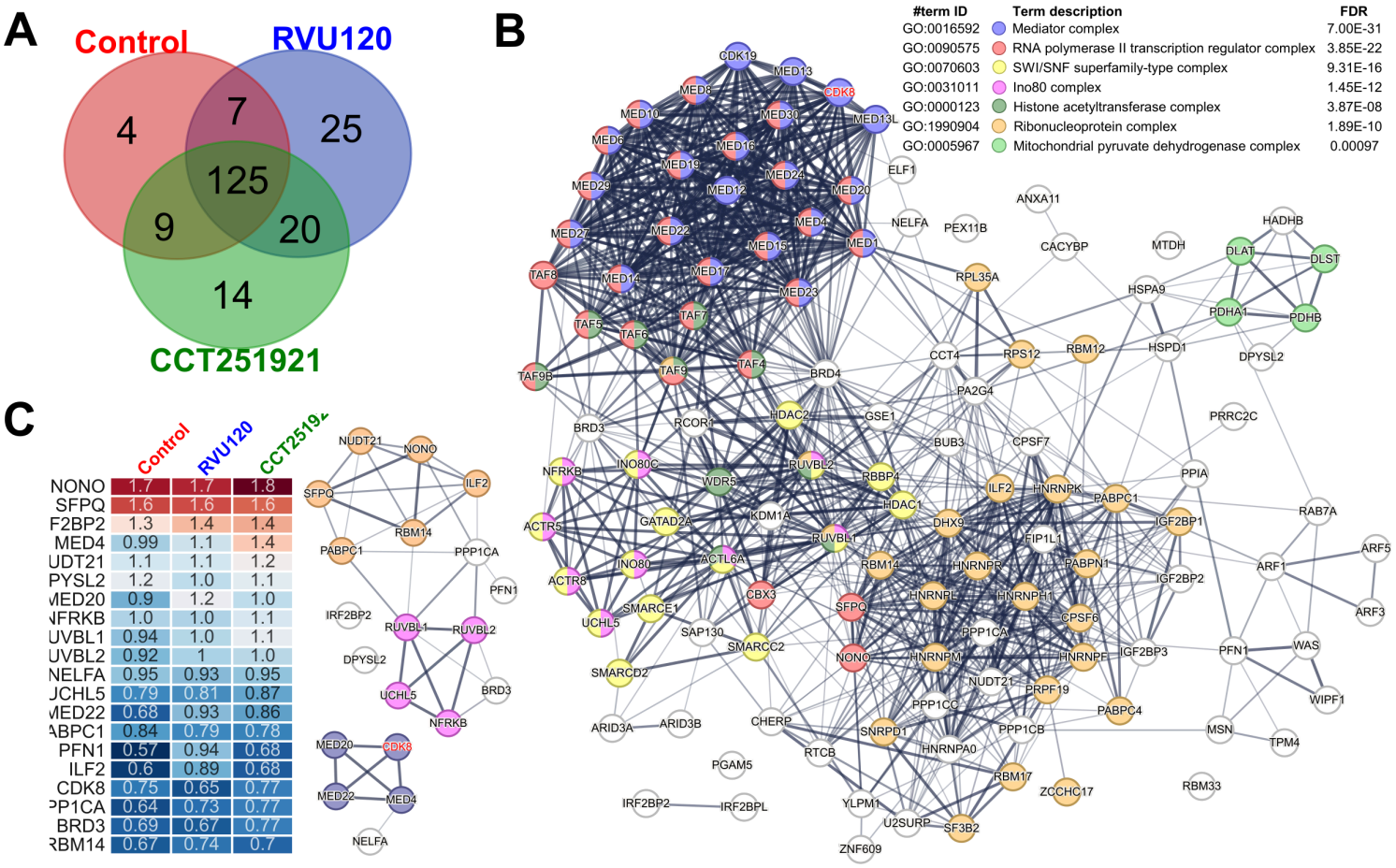

Figure 4

Proteomic characterisation of the CDK8 interactome in the TEX cell line. (A) Venn diagrams with numbers of identified CDK8 interacting proteins at control and 3h following the RVU120 and CCT251921 treatment in the TEX cell line. **(B)**String and functional analysis of 125 core CDK8-interacting proteins; line thickness indicates the strength of data support. The functional enrichment analyses were performed within the String tool using the Reactome database and the whole genome/proteome as the statistical background. **(C)** The list of 20 most abundant CDK8-interacting proteins in the TEX cell line and their interactions based on the STRING analysis. The semiquantitative abundances in the table are expressed as the APEX index.

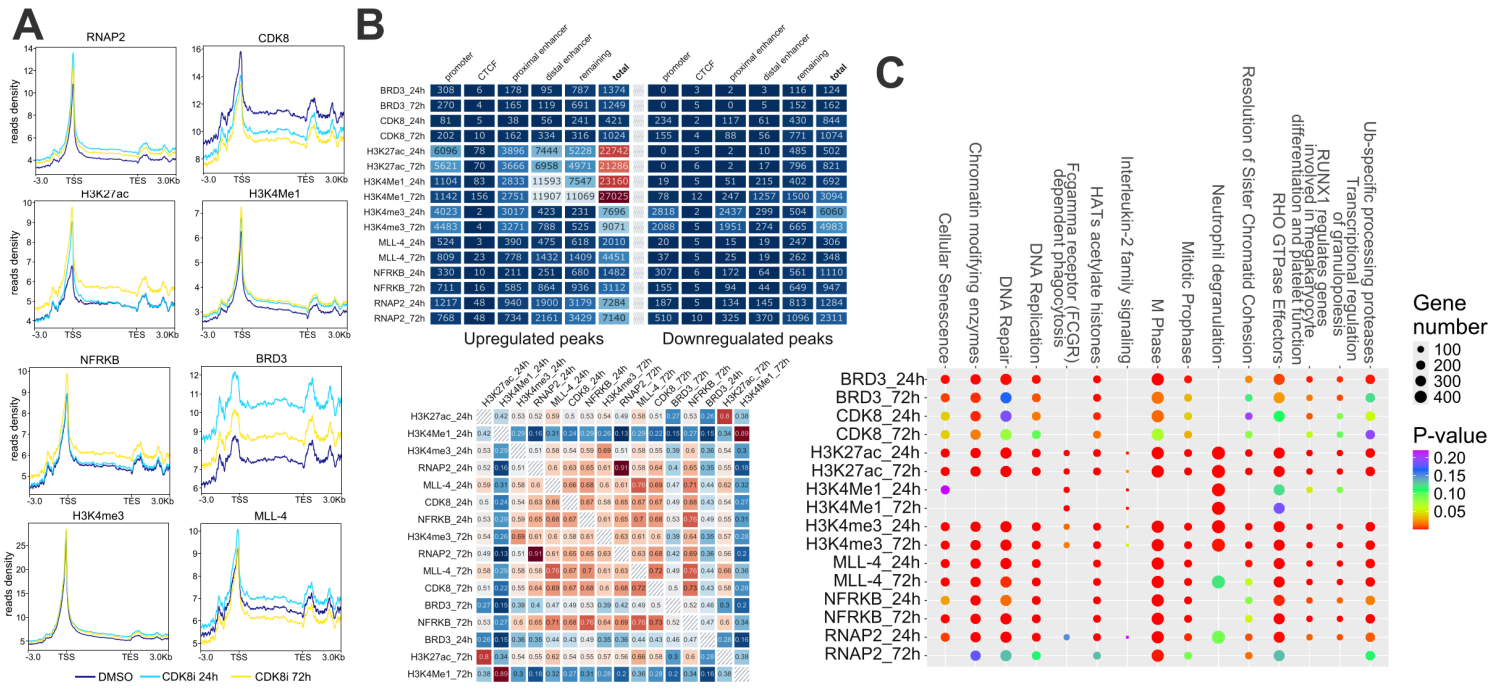

Figure 5

Genomic occupancy profiling reveals distinct chromatin remodelling programs following CDK8 inhibition. **(A)** Genome-wide distribution of CDK8, NFRKB, BRD3, RNAP2, MML4, and H3K27ac, H3K4me1, and H3K4me3 histone marks around transcription start sites (TSSs) and transcription end (TESs) in TEX cells following 24h and 72h CDK8 inhibition, illustrating loss of CDK8 binding and coordinated gain of signals for other factors after CDK8 inhibition. **(B)** Upper panel. Number of up- and downregulated MASC2 defined peaks (q-value ≤ 0.01) for each factor (BRD3, CDK8, H3K27ac, H3K4me1, H3K4me3, MLL-4, NFRKB, RNAP2) at 24 h and 72 h following CDK8 inhibition, stratified by genomic annotation (promoter, CTCF, proximal enhancer, distal enhancer). Lowe panel. Pairwise Pearson correlation matrix of genomic occupancies for CDK8, RNAP2, NFRKB, BRD3, MLL4 and histone marks (H3K4me1, H3K4me3, H3K27ac) at 24 h and 72 h after CDK8 inhibition, revealing a tightly correlated MLL4–RNAP2–CDK8–NFRKB network and a distinct H3K4me1 enhancer program with weaker coupling to the transcriptional machinery. **(C)** Dot plot of Reactome pathway enrichments for differentially bound regions across CDK8, RNAP2, NFRKB, BRD3, MLL4 and histone marks (H3K4me1, H3K4me3, H3K27ac) in CDK8 inbibitors treated TEX cells at 24h and 72h versus control. Dot size represents gene count (100-400 genes/pathway), while color indicates -log10(p-value), with red for highly significant enrichments and blue for less significant ones.

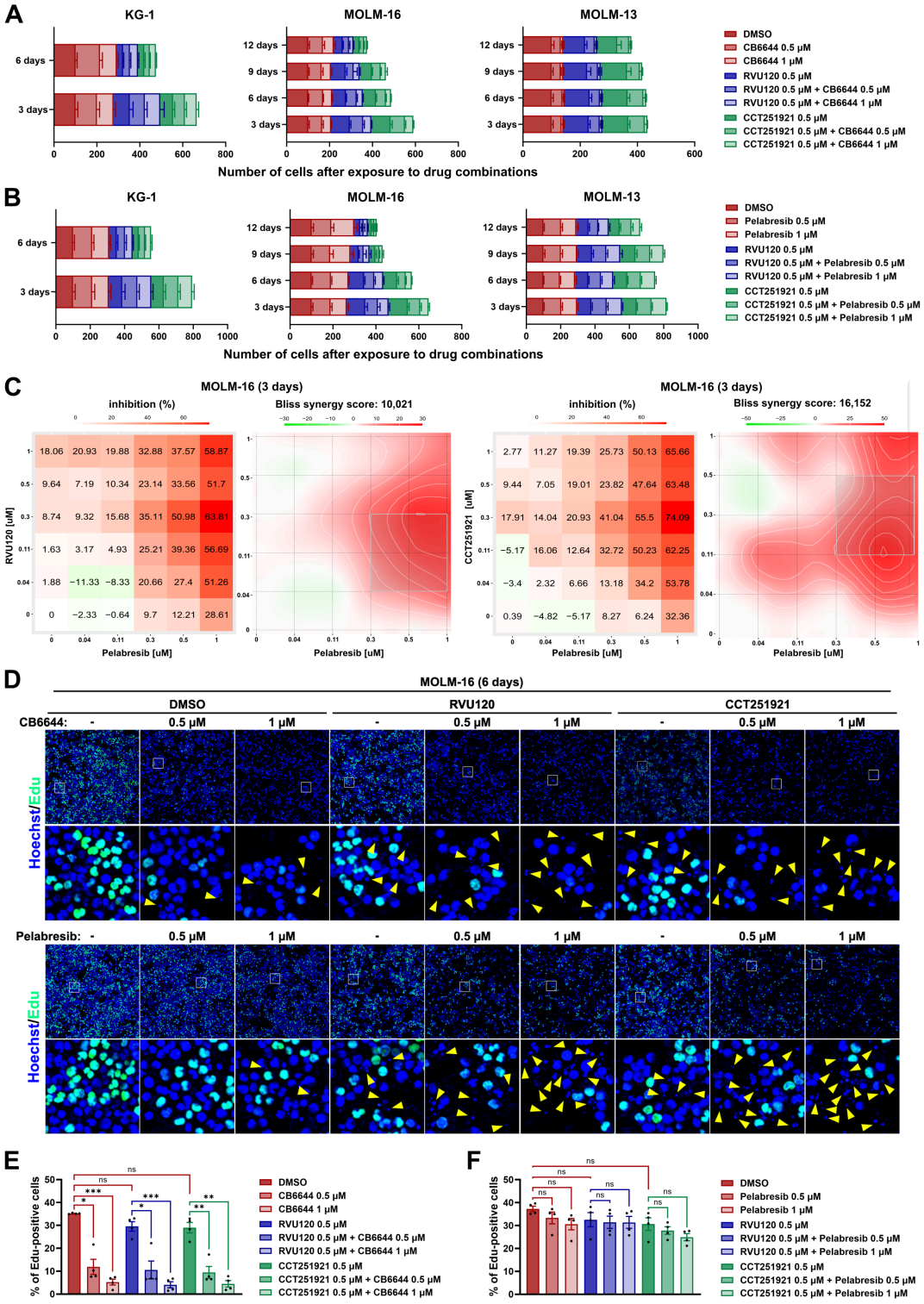

Figure 6

BET inhibition with Pelabresib acts synergistically with CDK8 inhibitors to potentiate their effects on MOLM-16 cell survival. (A-B) Bar graphs showing the results of high-content screening (HCS)-based analysis of KG-1, MOLM-13, and MOLM-16 cell growth upon treatment with DMSO or CDK8 inhibitors (RVU120 and CCT251921), alone or together with CB6644 (A) or Pelabresib (B). After exposure to the compounds at the indicated concentrations for the indicated days, live cell numbers were assessed

using HCS microscopy of Hoechst 33342-stained cells. **(C)** Dose response heatmap matrices of cell growth inhibition and synergy distribution visualisations showing the combined effects of treating MOLM-16 cells for 3 days with various concentrations of CDK8 inhibitors and Pelabresib. The calculated Bliss scores (+10.021 and +16.152, respectively) indicate synergy between RVU120 and Pelabresib (left) or CCT-251921 and Pelabresib (right). The analysis was performed using the Synergy Finder tool, based on HCS-assessment of live cell numbers. **(D)**Representative confocal microscopy images from the EdU incorporation assay in MOLM-16 cells treated for 6 days with DMSO, CDK8 inhibitors, Pelabresib or indicated drug combinations. Images were obtained by HCS confocal microscopy of cells stained with Hoechst 33342 dye (detecting DNA; blue), and with click-chemistry reagents (detecting Edu incorporated into replicated DNA; green). **(E-F)** Bar graphs showing the results of high-content screening (HCS)-based analysis of the percentage of Edu-positive cells (those that replicated their DNA) among live MOLM-16 cells treated with DMSO or CDK8 inhibitors (RVU120 and CCT251921), alone or together with CB6644 (E) or Pelabresib (F). Mean values (n=4 ± SEM) compared statistically as indicated on the graphs. P-values are highlighted as: ns ($P > 0.05$), * ($P < 0.05$), ** ($P < 0.01$) or *** ($P < 0.0001$).

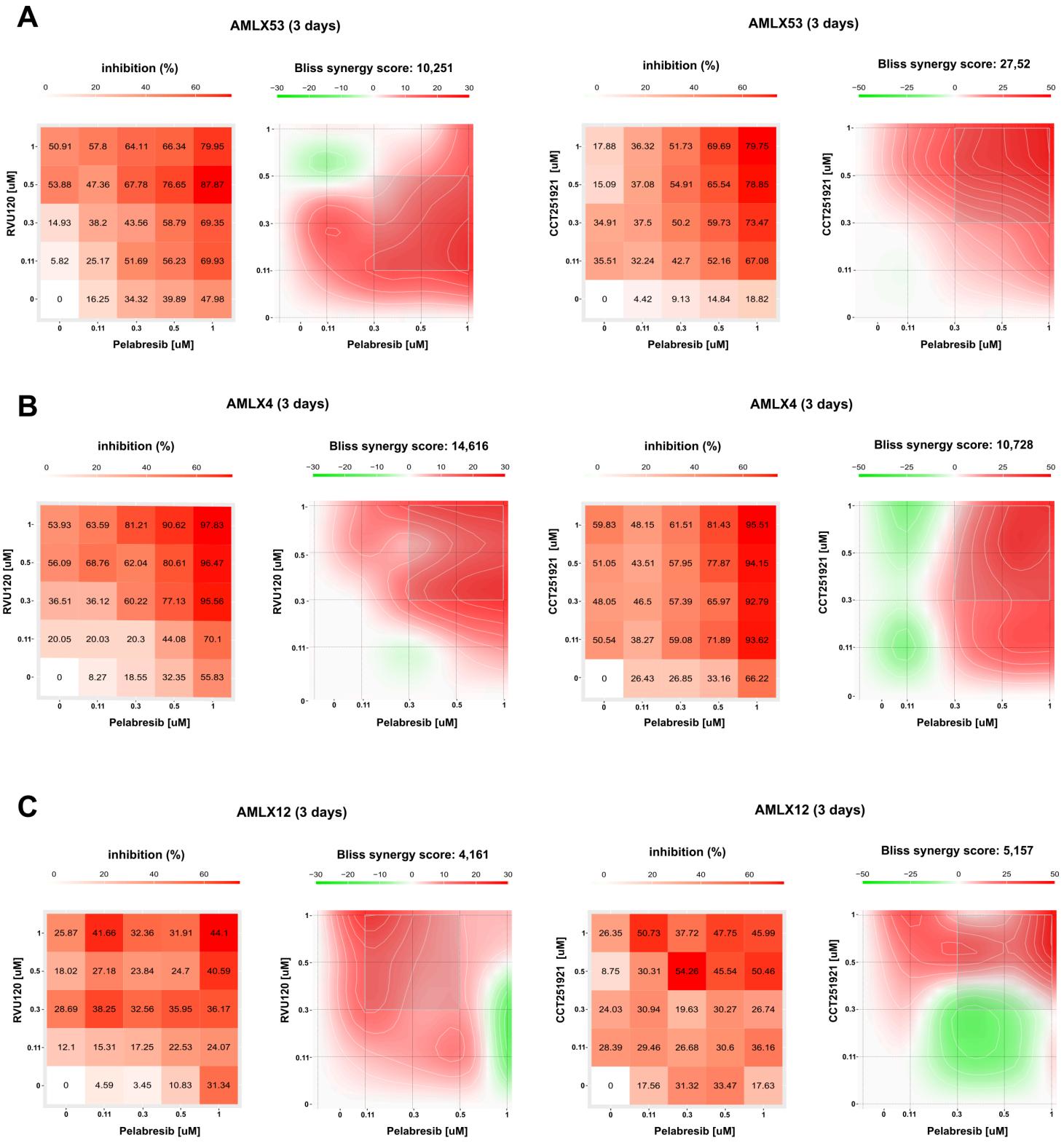

Figure 7

Synergy between BET and CDK8 inhibition can be observed in PDX AML models. (A-C) Dose response heatmap matrices of cell growth inhibition and synergy distribution visualisations, showing the combined effects of treating cells from three PDX AML models. The cells were treated with various concentrations of CDK8 inhibitors and Pelabresib for 3 days. The analysis was performed using the Synergy Finder tool, based on HCS-assessed live cell counts. The results indicate synergy between

RVU120 (left) or CCT251921 (right) and Pelabresib in AMLX53 and AMLX4 (Bliss scores > +10; shown in A and B) and additive effects between the two CDK8 inhibitors and Pelabresib in AMLX12 (Bliss scores > 0 and <+10, shown in C).

Supplementary Files

This is a list of supplementary files associated with this preprint. Click to download.

- Additionalfile1.pdf
- Additionalfile10.xlsx
- Additionalfile11.xlsx
- Additionalfile12.xlsx
- Additionalfile13.pdf
- Additionalfile14.xlsx
- Additionalfile15.xlsx
- Additionalfile16.xlsx
- Additionalfile2.xlsx
- Additionalfile3.pdf
- Additionalfile4.xlsx
- Additionalfile5.xlsx
- Additionalfile6.xlsx
- Additionalfile7.pdf
- Additionalfile8.pdf
- Additionalfile9.xlsx